



Master thesis

# Electrochemical Modeling of a Lithium Ion Cell

Submitted by  
Katja Fröhlich

In cooperation with  
Austrian Institute of Technology

Supervisor:  
Assoc.Prof. Dipl.-Ing. Dr.techn. Viktor Hacker

March 2013

## Danksagung

Diese Arbeit wäre ohne die Hilfe einiger Personen nicht entstanden, welchen ich an dieser Stelle danken möchte.

Mein besonderer Dank gilt Viktor Hacker vom Labor für Brennstoffzellensysteme an der Technischen Universität Graz für die Betreuung und die hilfreichen Anregungen zur Verfassung der Arbeit.

Ebenso möchte ich mich bei Robert Permann bedanken, der mich von Seiten des *Austrian Institute of Technology* hilfreich unterstützt hat. Auch Dragan Simic ist mir speziell im Hinblick auf Form und Layout der Arbeit zur Seite gestanden. Zusätzlich danke ich allen MitarbeiterInnen des *Mobility Departments* für die freundliche Aufnahme in das Team und das gute Arbeitsklima.

An dieser Stelle bedanke ich mich besonders bei meinen Eltern, die mich nicht nur während meines Studiums finanziell sowie auch seelisch unterstützt haben.

Diese Arbeit widme ich meinem Freund Philipp, der mir immer zur Seite gestanden ist und mir gleichzeitig genügend Freiraum zum Verfassen der Arbeit gegeben hat.

**STATUTORY DECLARATION**

I declare that I have authored this thesis independently, that I have not used other than the declared sources / resources, and that I have explicitly marked all material which has been quoted either literally or by content from the used sources.

.....  
date

.....  
signature

## Kurzfassung

Die wichtigsten Phänomene und chemischen Prozesse in einer Lithium-Ionen Zelle werden mathematisch beschrieben. Die hierzu verwendeten partiellen Differentialgleichungen und Randbedingungen für die verschiedenen Phasen des Modells wurden in COMSOL Multiphysics gelöst. Diese Software verwendet Finite Elemente Analyse zur Lösung des Modells. Bei dieser Methode wird das Modell in kleine Elemente unterteilt, in welchen die abhängigen Parameter näherungsweise berechnet werden können. Ein Parameterdurchlauf wird durchgeführt, um den Einfluss verschiedener Zelleigenschaften zu bestimmen.

Die Arbeit beginnt mit einer thematischen Einleitung. Nach dem Ausblick wird der theoretische Hintergrund näher erklärt. In diesem Teil wird zunächst die Arbeitsweise des Lithium-Ionen Akkumulators beschrieben. Verschiedene Zellmodelle werden verglichen und evaluiert. Die Diskretisierungsmethode, die Finite Elemente Analyse, wird ebenfalls erläutert. In Kapitel drei ist das Modell charakterisiert. Die Modellannahmen werden aufgelistet und die Geometrie sowie die Vernetzung beschrieben. Im nächsten Kapitel ist die Implementierung der Simulation in COMSOL Multiphysics dargestellt. Kapitel sechs zeigt die Resultate des dreidimensionalen Modells und des Parameterdurchlaufs. Schlussfolgerungen und weitere Ausblicke komplettieren die Masterarbeit.

## Abstract

Significant phenomena and main chemical processes in a lithium ion cell are mathematically described. The partial differential equations and boundary conditions for the different phases of the model are solved using COMSOL Multiphysics. This software uses finite element analysis as the method of discretization. This is a method which divides the model into small elements, in which the dependent parameters can be estimated. A parametric sweep is performed to evaluate the influence of different cell properties.

The thesis starts with a thematic introduction. After the outline, the theoretical background of the work is described. In this section, the operation principles of a lithium ion accumulator are specified. Different existing cell models are described, compared and evaluated. The method of discretization, the finite element analysis, is illustrated as well. In chapter three, the model is characterised. The model assumptions are listed and the geometry and meshing are described. In the next chapter, the simulation implementation in COMSOL Multiphysics is outlined. Chapter six figures the results of the three-dimensional model and the parametric sweep. Conclusions and further perspectives complete the master thesis.

# Table of Contents

1	Introduction . . . . .	1
1.1	Motivation . . . . .	1
1.2	Objective . . . . .	2
1.3	Outline . . . . .	3
2	Theoretical background . . . . .	4
2.1	Lithium ion battery . . . . .	4
2.2	Mathematical models for lithium ion batteries . . . . .	6
2.2.1	Empirical models . . . . .	6
2.2.2	Electrochemical models . . . . .	7
2.2.3	Multiphysics model . . . . .	9
2.2.4	Molecular model . . . . .	10
2.3	State-of-the-art battery modeling and experimental data . . . . .	11
2.3.1	Lithium concentration in the solid phase . . . . .	11
2.3.2	Lithium concentration in the liquid phase . . . . .	12
2.3.3	Cell geometry variation . . . . .	13
2.3.4	Multi-layer simulation . . . . .	14
2.4	Finite Element Method . . . . .	15
2.4.1	Method of discretization . . . . .	15
2.4.2	Mesh elements . . . . .	17
3	Model characterization . . . . .	19
3.1	Model assumptions . . . . .	19
3.2	Scheme and meshes . . . . .	20
3.2.1	Geometry . . . . .	20
3.2.2	Mesh elements . . . . .	21
4	Mathematical description of battery processes . . . . .	25
4.1	Electrolyte . . . . .	25
4.1.1	Mass transport and current distribution . . . . .	25
4.1.2	Conservation laws . . . . .	26
4.1.3	Electrolyte in the pores of the electrode . . . . .	27
4.2	Electrode particles . . . . .	28
4.2.1	Mass transport . . . . .	28
4.2.2	Electrode potentials . . . . .	28
4.2.3	Charge conservation . . . . .	30
5	Implementation in COMSOL Multiphysics . . . . .	31
5.1	The COMSOL environment . . . . .	31
5.1.1	Global definitions . . . . .	32

	5.1.2	Model . . . . .	32
	5.1.3	Study . . . . .	34
	5.1.4	Results . . . . .	35
5.2		Building a model . . . . .	35
	5.2.1	Model Wizard . . . . .	35
	5.2.2	Geometry . . . . .	36
	5.2.3	Variables, parameters and other definitions . . . . .	37
	5.2.4	Physics interfaces . . . . .	38
	5.2.5	Meshing . . . . .	39
	5.2.6	Study . . . . .	39
	5.2.7	Parametric sweep . . . . .	39
6		Results and discussion . . . . .	41
6.1		3D General model . . . . .	41
	6.1.1	Lithium concentration in the solid phase . . . . .	41
	6.1.2	Lithium concentration in the liquid phase . . . . .	43
	6.1.3	Lithium ion flux . . . . .	44
6.2		Particle radii variation . . . . .	45
	6.2.1	Lithium concentration in the solid phase . . . . .	45
	6.2.2	Lithium concentration in the liquid phase . . . . .	47
	6.2.3	Lithium ion flux . . . . .	47
6.3		Volume fraction variation . . . . .	48
	6.3.1	Lithium concentration in the solid phase . . . . .	49
	6.3.2	Lithium concentration in the liquid phase . . . . .	51
	6.3.3	Lithium ion flux . . . . .	52
6.4		Length variation . . . . .	53
	6.4.1	Lithium concentration in the solid phase . . . . .	53
	6.4.2	Lithium concentration in the liquid phase . . . . .	54
	6.4.3	Lithium ion flux . . . . .	55
7		Conclusions and further perspective . . . . .	57
	7.1	Conclusions . . . . .	57
	7.2	Further perspective . . . . .	58
A		Appendix . . . . .	G
	A.1	Parameter setup . . . . .	G
	A.2	Feature nodes . . . . .	H
		A.2.1 <i>Convection-Diffusion Equation</i> . . . . .	H
		A.2.2 <i>Transport of Diluted Species</i> . . . . .	H

# List of symbols

## Greek letters .

$\alpha$ .....	Charge transfer coefficient [ <i>none</i> ]
$\delta_{ij}$ .....	Kronecker delta [ <i>none</i> ]
$\epsilon$ .....	Volume fraction [ <i>none</i> ]
$\eta$ .....	Local coordinate [ <i>none</i> ]
$\Omega$ .....	Domain [ $m^3$ ]
$\phi$ .....	Basis function [ <i>none</i> ]
$\sigma$ .....	Electric conductivity [ $S m^{-1}$ ]
$\varphi$ .....	Electric potential [ $V$ ]
$\zeta$ .....	Local coordinate [ $m$ ]

## Roman letters

$A$ .....	Area [ $m^2$ ]
$a$ .....	Specific interfacial area [ $m^{-1}$ ]
<i>brugg</i> .....	Bruggemann correction factor [ <i>none</i> ]
$c$ .....	Concentration [ $mol m^{-3}$ ]
$D$ .....	Diffusion coefficient [ $m^2 s^{-1}$ ]
$E$ .....	Electric field [ $V m^{-1}$ ]
$F$ .....	Faraday constant = 96 485.34 [ $s A mol^{-1}$ ]
$H$ .....	Height [ $m$ ]
$I$ .....	Current [ $A$ ]
$J$ .....	Flux density [ $mol s^{-1} m^{-2}$ ]
$j$ .....	Current density [ $A m^{-2}$ ]
$k$ .....	Reaction rate constant [ $s^{-1}$ ]
$L$ .....	Length [ $m$ ]
$n$ .....	Normal vector [ <i>none</i> ]
$R$ .....	Universal gas constant = 8.314 [ $J mol K^{-1}$ ] Electrical resistance [ $\Omega$ ]

	Particle radius [ $m$ ]
$r$ .....	Reaction rate [ $molm^{-3}s^{-1}$ ]
$s$ .....	Surface [ $m^2$ ]
$T$ .....	Absolute temperature [ $K$ ]
$t$ .....	Time [ $s$ ]
$U$ .....	Voltage [ $V$ ]
$u$ .....	Dependent variable [ <i>several</i> ]
$x$ .....	Global coordinate [ $m$ ]
$z$ .....	Ionic charge [ <i>none</i> ]
<b>Subscript</b> .....	
0 .....	Standard or initial
$a$ .....	Anode
$app$ .....	Applied
$b$ .....	Binder material
$c$ .....	Cathode
$cell$ .....	Cell
$d$ .....	Diffusion
$eq$ .....	Equilibrium
$i$ .....	Replacement character
$l$ .....	Liquid phase
$Li^+$ .....	Lithium ion
$m$ .....	Migration
$max$ .....	Maximum
$PF_6^-$ .....	Hexafluorophosphate ion
$s$ .....	Solid phase
$sep$ .....	Separator
$sf$ .....	Surface
$tot$ .....	Total
$x$ .....	Local

# 1 Introduction

## 1.1 Motivation

Environmental matters are one of the most important issues of our time. The reduction of pollutant emissions, caused by power generation, industries and transportation, is in great demand and some sanctions have already been intended. The observation of electric energy from renewable resources, for example, is a great step forward to diminish air pollution. Nevertheless, the power generated from wind, water and other resources mostly isn't constantly available and if, has to be transported to where electric energy is needed. These issues ask for a portable energy storage system, like lithium ion batteries. Lithium ion batteries are already in use in various portable devices like mobile phones, laptops and other small electronic equipment. Their high power density, lightweight and decreasing costs, make these battery systems an promising candidate for application in electric vehicles as well [1], [2].

Electric engines have several advantages compared to combustion engines

- Zero emission during the conversion of energy into propulsion
- Noise reduction
- High energy density
- High efficiency
- Maximum torque from 0 rpm

The disadvantages are

- Long charging time
- Short driving range
- Size and weight restrictions

Therefore it is necessary to improve battery design and materials in order to improve the performance of lithium ion batteries and further electric vehicle concepts [3].

To reach this target, a lot of cell testing is necessary. Cell tests are not only time consuming but also quite expensive due to abrasion of material and equipment. Additionally, some phenomena inside the cell and behaviour of the battery under limited conditions are not measurable. These aspects make electrochemical modeling reasonable and meaningful. Modeling lithium ion batteries gives a great insight in the cell and shows cell behaviour and profiles which would not be accessible in another way.

## **1.2 Objective**

The aim of the thesis is to build up a three-dimensional electrochemical model of a conventional lithium ion cell. In aspect to simulation time and the cost of a detailed multiphysical model, a model should be sufficiently accurate without being more elaborate than necessary [4]. The developed model is an example for a simple model as a starting point for further extensions, depending on the objectives and application field. Significant phenomena and chemical processes are described mathematically and the concerning equations are solved using finite element analysis by COMSOL Multiphysics. The results are concentration profiles, electric potentials and fields and current density distribution inside the lithium ion cell. Additionally, some cell parameters are varied to validate their influence and the sensitivity of the model.

## 1.3 Outline

After the introduction, in the second chapter of the thesis, the functionality of a lithium ion cell is described. The theoretical background also includes the description of different existing models with different levels of complexity and their application areas. The finite element analysis as the equation solving method is explained in the third part of chapter two.

In the next chapter, the considered processes in the electrochemical cell are listed. The chemical description involves conservation laws, transport processes and reaction kinetics. The assumptions made to reduce the complexity of the model are described in the next part. The geometry and the meshing of the cell is described at the end of chapter three.

The processes taken into account are described mathematically in chapter four; there is already a wide range of various equations in the literature, like [5], [6] and [7], to mention just some of them. Then the needed parameter values are defined, some values are taken from the literature and some are assumed.

Chapter five describes the procedure of simulating in COMSOL Multiphysics and the implementation of the so-called parametric sweep. Boundary and domain conditions, as well as other settings and features of the model are described here.

The simulation results are delineated in chapter six. First, the electrochemical model with the fixed parameter values is presented. Then the influence of various parameters is shown and discussed.

At the end of the thesis, a short summary of the main results and a conclusion of the project is done. Further perspectives on the electrochemical modeling will be made to round up the thesis.

## 2 Theoretical background

### 2.1 Lithium ion battery

The lithium ion cell consists of two porous electrodes, a mostly liquid electrolyte and a separator. The main components of the electrolyte are ethylene carbonate (EC), dimethyl carbonate (DMC) or ethylmethyl carbonate (EMC) as the main organic solvent and 1 M lithium hexafluorophosphate ( $\text{LiPF}_6$ ) as the salt. The separator is needed to prevent shorting of the cell and allows ions to pass through its porous structure. The negative electrode consists of carbonaceous material and the positive electrode is mostly a metal oxide where the lithium ion could intercalate. The positive current collector is typically made of aluminium while the negative current collector is made of copper. In a conventional lithium ion battery, the current collectors have active electrode material on both sides and the battery consists of various layers of electrodes and separators (see figure 2.1) [1].

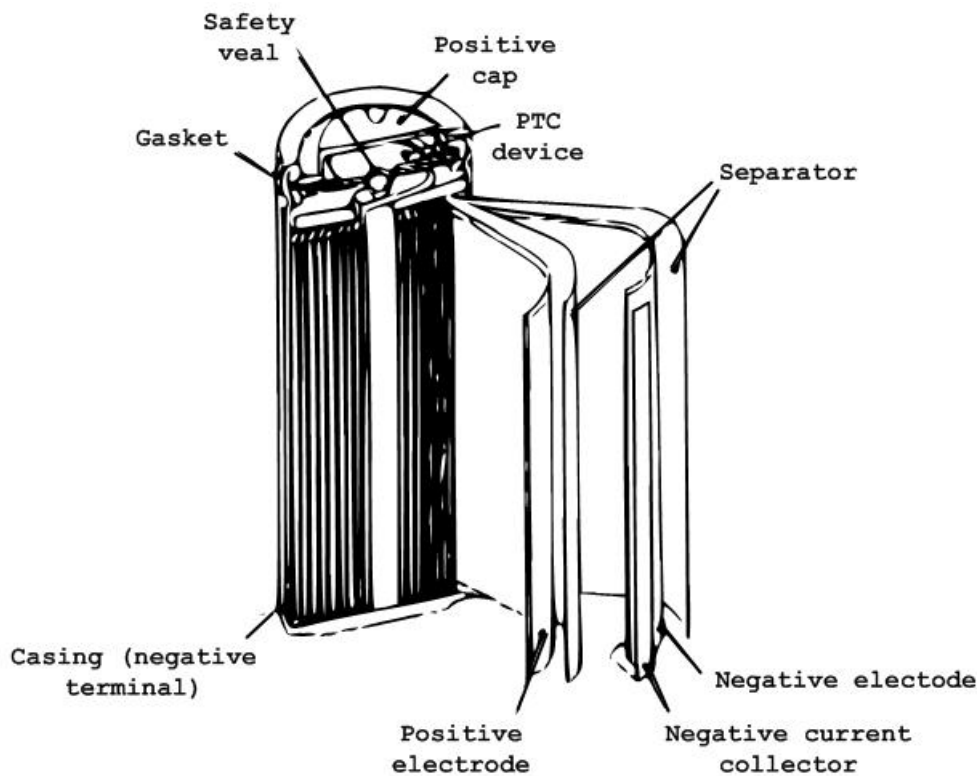
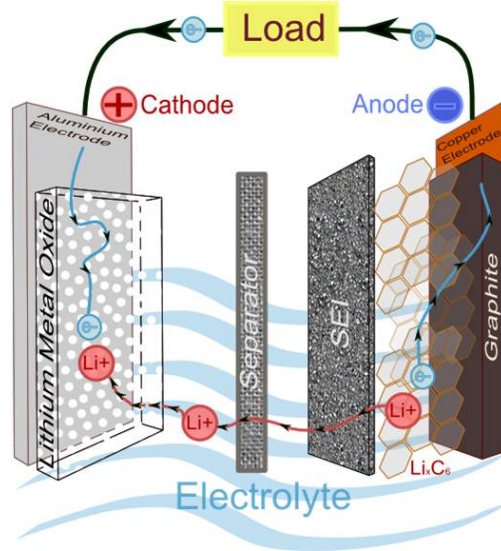


Figure 2.1: Scheme of a conventional lithium ion battery [8]

While discharging of the cell, lithium is de-intercalated from the negative electrode and chemically reacts at the surface of the particle (see figure 2.2). The thereby arisen lithium ion now passes through the interface between the solid phase and the electrolyte. Meanwhile the electron migrates through the conductive electrode material to the current collector of the electrode. After passing the interface, the lithium ion gets solvated in the electrolyte and moves through the separator holes to the positive electrode. At the interface of the positive electrode, the solvation sheath and the lithium ion divide. After the breakup, the lithium ion diffuses to the surface of the positive electrode particle, where it meets the electron, which has migrated from one current collector to the other via an external loop and closes the circuit. The components react again and the product is intercalated at the electrode. While charging, the procedure is taking place vice versa. The transport of lithium from one electrode to the other is the so-called 'rocking-chair' effect [1].



**Figure 2.2: Discharge process of a lithium ion cell**

At the negative electrode during discharge:



At the positive electrode during discharge:



## 2.2 Mathematical models for lithium ion batteries

Many different types of mathematical models for batteries exist and are published frequently. The difference between the models is mainly their complexity and according to this, computation time as well. The more complex a model is, the bigger is the insight of the processes in the cell and their components and the higher is the reliability on the predictions. In this thesis is distinguished between empirical models, electrochemical models, multiphysics models and molecular models.

### 2.2.1 Empirical models

Empirical models are build up from experimental data without concerning electrochemical or physical properties. The big advance of these models is that they have much faster calculation time than all other models and are easy to handle. Empirical models can not be used for new battery design applications and their predictions can be very poor for miscellaneous operating conditions [4].

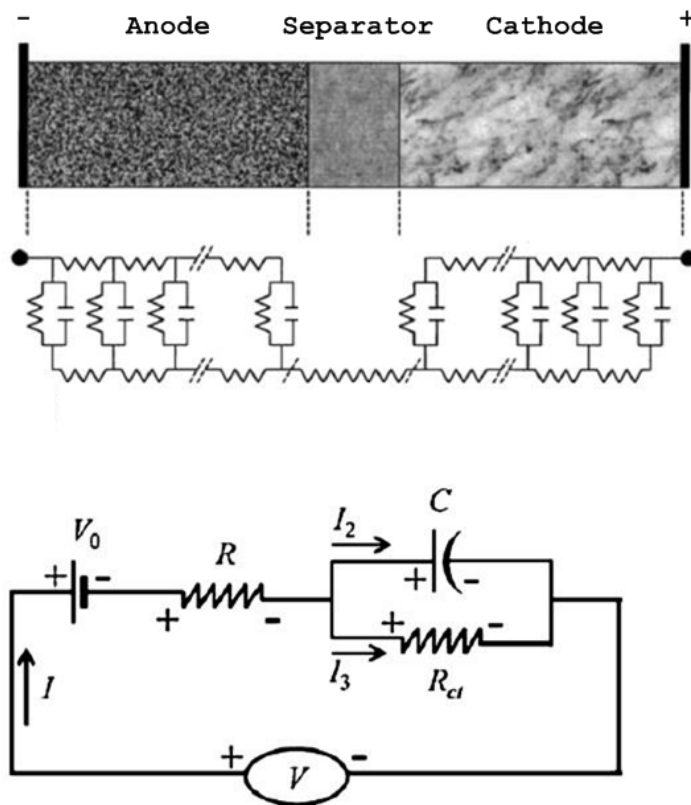


Figure 2.3: Electronic network for a lithium ion cell [9]

### *Equivalent circuit*

Equivalent circuit models consist of an electronic network with passive and/or active elements, for example capacitances, resistances, voltage sources, inductances and others (see figure 2.3). The required parameters, the element values, are fitted with experimental data [10].

### *Semi-empirical model*

This model type is a mixture of the usage of a set of equations to describe mathematically the cell behaviour, and parameters which have to be estimated or fitted with experimental data. The concerning equations reach from quite similar to first principle approaches to polynomial, exponential or other simple functions. Even if some developers claim to extrapolate the model data to other conditions as well, the reliability is questionable [11].

## **2.2.2 Electrochemical models**

Electrochemical models describe mathematically transport processes, species and charge conservation and chemical kinetics. Various kinds of electrochemical models exist, each of them describing the electrochemical processes in the lithium ion cell sufficiently accurate and making assumptions to reduce the computational solution time. The importance of the assumptions is very high and their applicability has to be checked carefully to ensure that the final results make sense [7].

### *Pseudo 2D model*

For simplification, the pseudo 2D model has two different length scales: the first is the thickness of the cell and the second along the particle radius (see figure 2.4). Homogeneous conditions over the cross section are assumed. The electrode materials are described as spherical particles, in which the diffusion of lithium is modeled. At the anode, two fluxes are considered: one for the intercalation of lithium and another for the reduction of the solvent at the electrode-electrolyte interface. This film formation over carbon particles is assumed to be the single cause for capacity fade. The thickness is related to the side reaction flux. The model assumes equal concentration of lithium over the particle surfaces and a constant diffusion coefficient for each control volume. When solving the equations, the lithium concentration in the particles has to be calculated for each point along the y coordinate, while the solution phase concentration and potentials are assumed to be constant. The separator resistance is neglected [12], [13].

### *Single particle model*

In this model, both electrodes are replaced by one spherical representative particle (see figure 2.4), whose area is equivalent to the whole active area of the solid phase in the electrode. The electrolyte concentration as well as the potential is assumed to be uniform. No side reactions, for example electrolyte decomposition or film formation at the interfaces, are considered. Therefore, capacity fade due to these phenomena cannot be predicted. Intercalation of lithium is the only phenomenon regarded and is described by a single diffusion process. Positive and negative electrode potentials are assumed to be solely time-dependent. The current distribution along the particle is assumed to be uniform. This model needs little calculation time but is only valid for thin electrodes and low rates [14], [15], [16], [17].

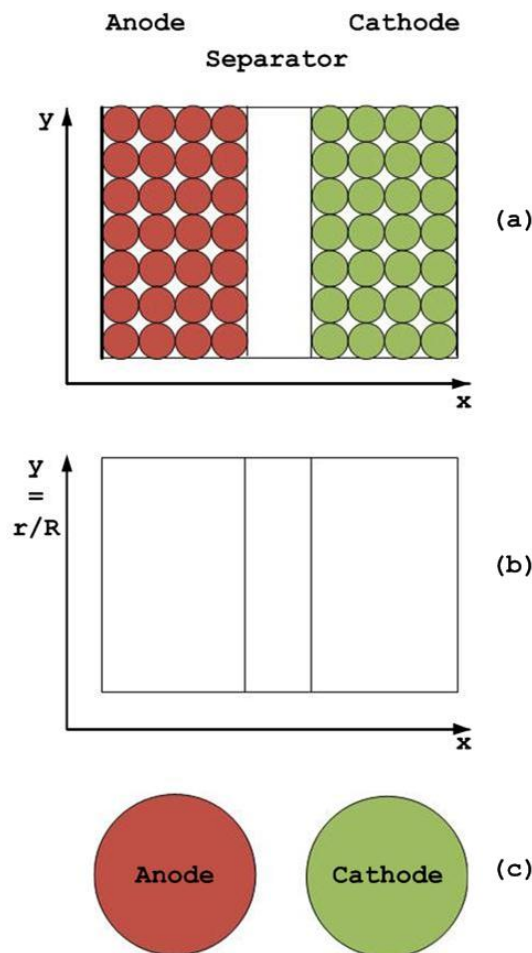


**Figure 2.4:** Schematic view of the three different models: (a) pseudo 2D model (b) rigorous model and (c) single particle model

### *Porous electrode model*

The so-called porous electrode model is a rigorous model, mainly presented and further improved by Newman et al. [18], [5]. The electrodes are considered to be superimposed continua of electrolyte, conductive material and active particles (see figure 2.4), so that diffusion of the lithium in the pore-filling electrolyte of the electrode is assumed to occur in parallel with the diffusion in the active particles. Volume averaging is performed; the solution and the matrix are assumed to be present at any point in the electrode space. Therefore, the parameters and the concentration variation of the liquid phase as well as the solid phase of the electrodes, are adjusted by the volume fraction of each phase. The transport of lithium ions through the interface is described by the Butler-Volmer equation. The Butler-Volmer equation is valid if the transport and chemical reaction is fast compared with the charge transfer through the interface. But at very high currents, transport of the reactants and products can be limited. In this case, other equations, describing the lithium transport outside the particles, are used. The electrolyte solution is modeled separately, using concentrated solution (mostly) or dilute solution theory. In the concentrated solution theory, the equations describing the transport of  $\text{Li}^+$  and  $\text{X}^-$  are similar to Stefan-Maxwell ones. In the dilute solution theory, interactions between the solute species are neglected [5], [19], [20].

### **2.2.3 Multiphysics model**

Multiphysics, multi-scale and multidimensional models exist in manifold ways. Previously described models have been isothermal. Especially for high power applications, adding a thermal model into an electrochemical approach is reasonable and makes sense. Multiphysics models are necessary for predicting cell behaviour under real operating conditions, for example in electric vehicles. But thermal and electrochemical modeling needs a lot of computational resources and is therefore decoupled in most cases [4].

Intercalation and deintercalation of lithium means volume change in the electrodes, causing stresses in the particles and may also lead to cracking of the material. These stresses, which are non-uniform across the particle, cause the loss of active material. This kind of modeling at the mesoscale (higher than molecular level and smaller than cell level) gives an insight in the active electrode material which can not be obtained in another way [21].

#### **2.2.4 Molecular model**

At the atomistic scale, phenomena are simulated which could not be obtained in another way. These simulations give explanations for various effects. The formation process of the solid-electrolyte interphase, for example, is one of the main reasons for capacity fade within the first cycles. New studies have shown that cracking of the active particles, caused by the intercalation and deintercalation process, lead to a new formation process which further reduces the capacity. Also the effect of different crystal structures and different electrode materials on the cell behaviour are predicted using molecular dynamics simulations. The free energy and the lattice structure of the molecules are calculated and their influence on the performance can be validated [4], [22], [23].

## 2.3 State-of-the-art battery modeling and experimental data

As mentioned in the last section, different types of models exist. The electrochemical model in this approach is close to Newman's *Porous electrode theory* and *Dilute solution theory*, which nowadays are one of the most accurate models regarding to describe electrochemical phenomena inside the cell. It is used to describe concentration changes, molar fluxes and current distribution, similar to those shown in this thesis. Newman's model has been used, validated and further improved by various scientists [24], [6], [20].

### 2.3.1 Lithium concentration in the solid phase

According to the *Porous electrode theory*, the transport of lithium in the solid phase of the electrodes is described by Fick's law of diffusion, an equation which doesn't contain any microstructural information about the electrode material. *In situ* measurements of the intercalation process of the anode have shown that the lithium first intercalates at the side of the electrode, which is exposed to the separator and close to the counter electrode. It is reasonable to expect the cathode to intercalate the lithium at this side of the electrode as well

The colours have been enhanced by graphical software for better visibility (see figure 2.5) [25].

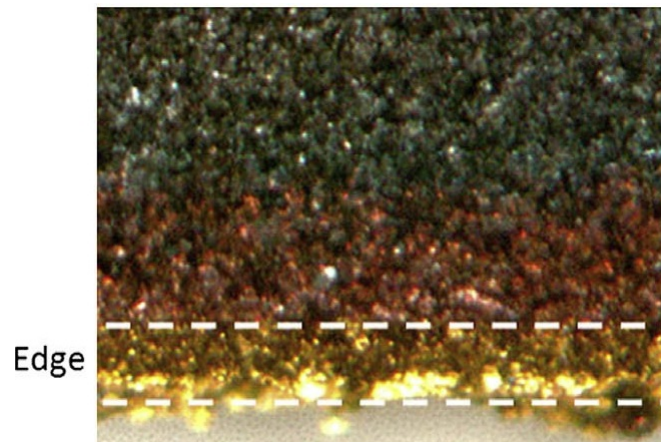


**Figure 2.5:** State of lithium intercalation after 45 minutes of charging [25]

Nevertheless, colours are only semi-quantitative and don't give detailed information about the concentration of intercalated lithium. Even though the data fit fairly the chronoamperometric data, obviously more detailed informations are needed.

### 2.3.2 Lithium concentration in the liquid phase

The one-dimensional transport of ions in the electrolyte is described by *Dilute solution theory* via [24]

$$\epsilon_k \frac{\partial c_i(x, t)}{\partial t} = \frac{\partial}{\partial x} \left( D_{eff} \frac{\partial c_s(x, t)}{\partial x} \right) + a(1 - t_+) \mathbf{J}(x, t) \quad (2.3)$$

The electrolyte phase concentration is approximated using *Garlekin's approximation*. In this method, basis functions that are satisfying the boundary conditions are chosen and the solution is approximated by a combination of the chosen basis functions. This procedural method seems quite similar to the way of discretization used by the *Finite element analysis* [24].

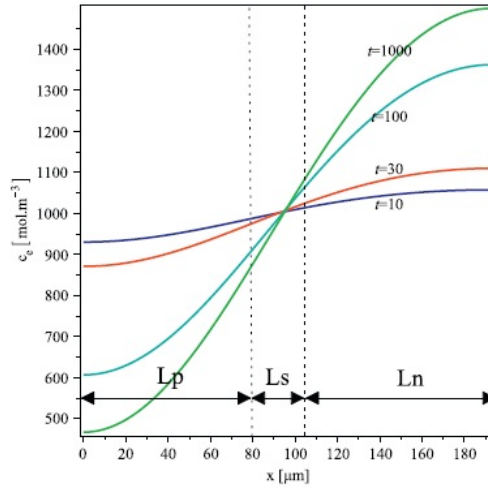


**Figure 2.6:** Lithium ion concentration in the electrolyte after 1 C of discharge [24]

According to the results, even after 10 seconds of discharging, the concentration varies significantly in the cell. The ion concentration rises at the electrode where the lithium is de-intercalated (here: anode) and drops at the counter electrode, where the lithium is intercalated (here: cathode) (see figure 2.6).

The results are similar to those presented by *V. Zadin et al.*, who calculated the concentration profile using a general diffusion-migration equation [26].

### 2.3.3 Cell geometry variation

V. Zadin and D. Brandell simulated variation of electrode lengths and distances between the electrodes of 3D-microbatteries. The concentration and potential in the electrolyte was calculated using *Nernst-Planck equation* and *Ohm's law*. This approach mostly compared polymer and liquid electrolytes, but also showed how the distance between the electrodes influences the concentration profile of the electrolyte (see figure 2.7) [27].

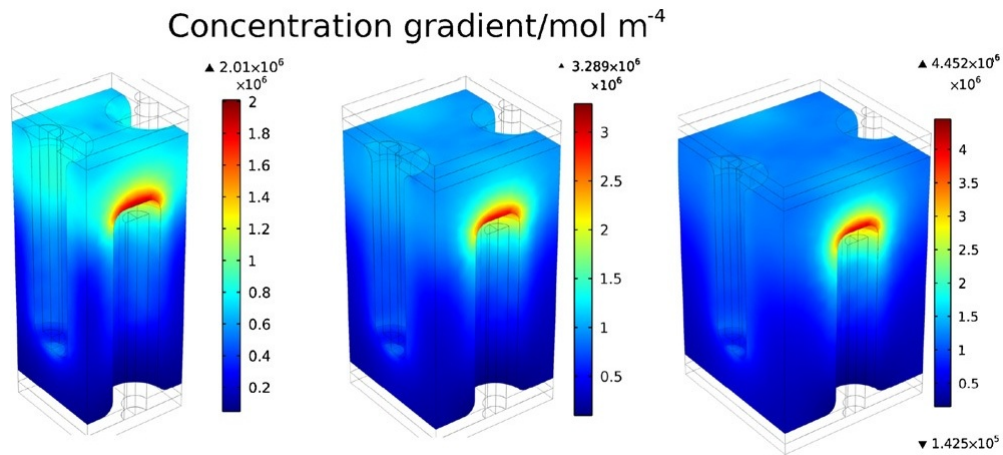


**Figure 2.7:** Concentration gradient in the electrolyte for different electrode distances [27]

It has been shown that the concentration differs strongly if the distance between the electrodes is smaller, and less for the larger region.

### 2.3.4 Multi-layer simulation

Among other things, *Y.-H. Chen et al.* simulated the effect of porosity on the electronic and ionic conductivity and battery performance (see figure 2.8) [28].

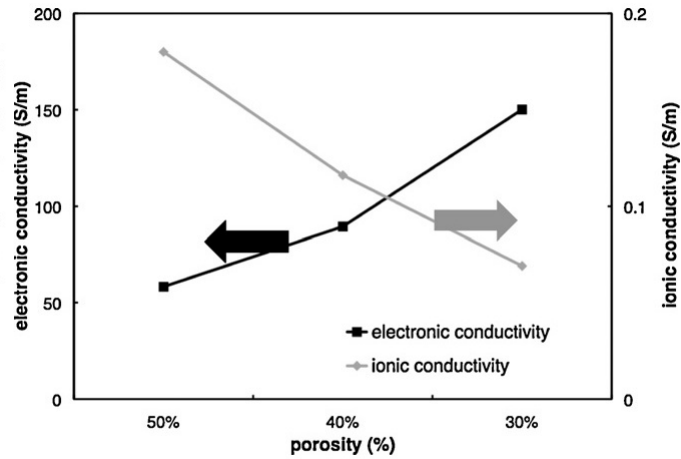


**Figure 2.8: Influence of the porosity on the ionic and electronic conductivity [28]**

As expected, the ionic conductivity of the electrode is directly related with the porosity, and the electronic conductivity drops for greater numbers and vice versa. This is reasonable, because the electrolyte fills the pores of the electrode and is highly conductive for ions, while the solid phase is the electronic conductor.

Therefore, the effect of the porosity of the electrode on the battery performance is high and the variation of this parameter gives more detailed information.

## 2.4 Finite Element Method

The finite element analysis is an approximation method that divides a model into small (finite) elements in which it is possible to determine the values of the dependent variables. This basic approach is widely used for different applications and various software programs, solving different engineering problems with the finite element method, exist. The rapid increase of the usage of the finite element analysis directly correlates with the evolution of hardware and software. It has converted from a method solely for experts in mathematics to a popular tool for various engineering applications. But even if software programs like COMSOL Multiphysics are user-friendly and easy-to-use, a fundamental knowledge of the method is essential to reduce errors and gain better insight into the software [29].

### 2.4.1 Method of discretization

Considering an independent variable  $u$  on an interval with a finite number of node points  $x_i$ . This variable can be approximated by a set of functions and parameters:

$$u^{(n)}(x) = \sum_{i=1}^n u_i \phi_i(x) \quad (2.4)$$

The degrees of freedom are the number of parameters  $n$ , which are used to express the dependent variable. The reliability of the solution but also the computational time depend strongly on the degrees of freedom [30].

The finite element space is specified by its basis functions  $\phi_i$ . Basis functions should be linearly independent, continuously differentiable and observe boundary conditions. Specifically,  $\phi_i(x)$  fulfills  $\phi_i(x_i)=1$  and  $\phi_i(x \neq x_i)=0$  for other node points (see figure 2.9). The order of the basis functions can be linear, quadratic or higher. The order of the function  $u$  correlates directly with the order of the basis function set and the higher the order of the basis function, the more node points are needed [31].

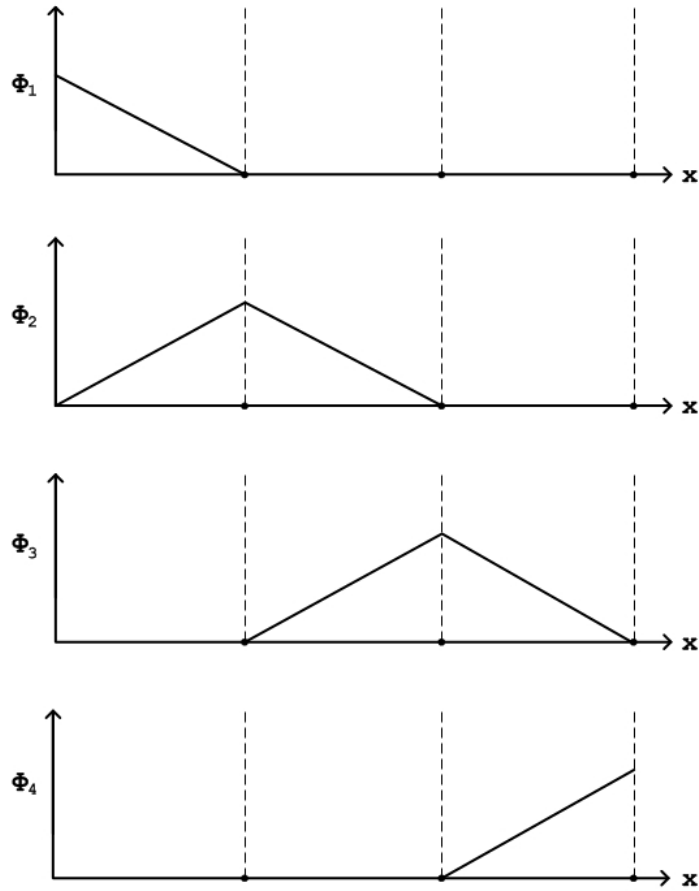


**Figure 2.9: Linear basis function set on an interval with four node points**

To define the so-called shape functions, local coordinates  $\zeta_j$  are introduced. The global coordinates  $x_i$  are functions of the local coordinates:

$$x_i(\zeta_j) = \sum_i \phi_i(\zeta_j) \quad (2.5)$$

For the local coordinates it is imperative that  $\sum_{i=1}^d \zeta_i = 1$ . The relation between the local coordinates and the global coordinates is shown in figure 2.10. In this figure, the global coordinates are  $x$  and  $y$ , while the local coordinates are  $\zeta$  and  $\eta$ , the model is two-dimensional.

With the set of shape functions, the basis functions for each node point can be constructed to approximate the function  $u(x)$  (see equation 2.4).

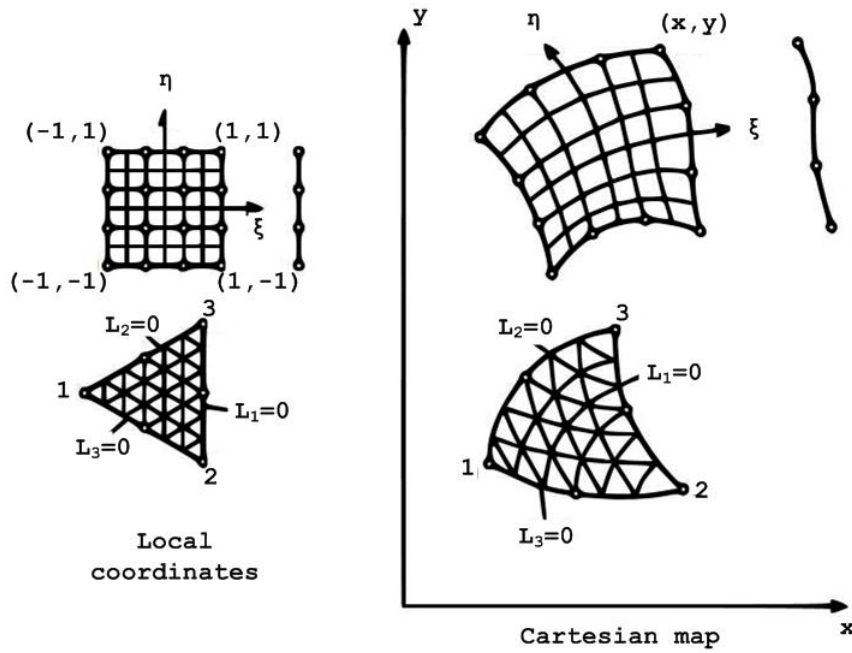


Figure 2.10: Connection between local and global coordinates [32]

### 2.4.2 Mesh elements

Lots of different mesh elements are available in COMSOL Multiphysics. The most important mesh elements are the Lagrange element, which is applied here, and the curved mesh element. The curved mesh element is useful to minimize the error due to curved boundaries. Since no curved boundary exists in the electrochemical model introduced here, the curved mesh element is not applied. The Lagrange element is the most common element type and available at all user interfaces of the software [31].

In this model, tetrahedral and triangular mesh elements are applied and the basis functions are quadratic (see figure 2.11).

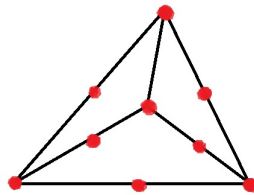


Figure 2.11: Lagrange element - Quadratic tetrahedron

Mesh elements are specified by their basis function set. The basis functions of the Lagrange element are determined by [33]

$$\phi_i(x_j, y_j) = \delta_{ij} \quad (2.6)$$

The applied shape space of the three-dimensional model has a basis of 10 quadratic shape functions (see table 2.1).

**Table 2.1: Shape function set of the Lagrange element**

Node point	Shape function
(0,0,0)	$(1 - \zeta_1 - \zeta_2 - \zeta_3)(1 - 2\zeta_1 - 2\zeta_2 - 2\zeta_3)$
(0.5,0,0)	$4\zeta_1(1 - \zeta_1 - \zeta_2 - \zeta_3)$
(0,0.5,0)	$4\zeta_2(1 - \zeta_1 - \zeta_2 - \zeta_3)$
(0,0,0.5)	$4\zeta_3(1 - \zeta_1 - \zeta_2 - \zeta_3)$
(0.5,0.5,0)	$4\zeta_1\zeta_2$
(0.5,0,0.5)	$4\zeta_1\zeta_3$
(0,0.5,0.5)	$4\zeta_2\zeta_3$
(1,0,0)	$\zeta_1(2\zeta_1 - 1)$
(0,1,0)	$\zeta_2(2\zeta_2 - 1)$
(0,0,1)	$\zeta_3(2\zeta_3 - 1)$

## 3 Model characterization

### 3.1 Model assumptions

These assumptions are made to simplify the model and reduce calculation time. Most of them consider a graphite anode, cobalt oxide ( $\text{CoO}_2$ ) cathode and an organic solvent with lithium hexafluorophosphate ( $\text{LiPF}_6$ ) salt as the electrolyte, but might be also valid for other materials as well.

- No convection within the cell (no fluid motion)
- No side reaction or solvent reduction
- One-step reaction:  $\text{Li} \rightarrow \text{Li}^+ + \text{e}^-$
- No volume changes (no mechanical stresses)
- Diffusion coefficient is constant in the electrolyte and in the particles
- The intercalation process is a single solid diffusion process
- Conductive additives are neglected in the calculation, the electrode particles are taken as conductive
- The processes are isothermal and isobaric
- The electrode particles are spherical and monodisperse
- The resistance of the separator is neglected
- The reaction is of first order
- The dissolved salt in the electrolyte is completely dissociated
- The anode is grounded ( $\varphi_a = 0$ )

## 3.2 Scheme and meshes

### 3.2.1 Geometry

The geometry of the model is held simple and can easily be applied to different battery geometries (see figure 3.1 and 3.2). The spirally wounded and the pouch cell are examples, other types like cylindrical ones could also be considered.

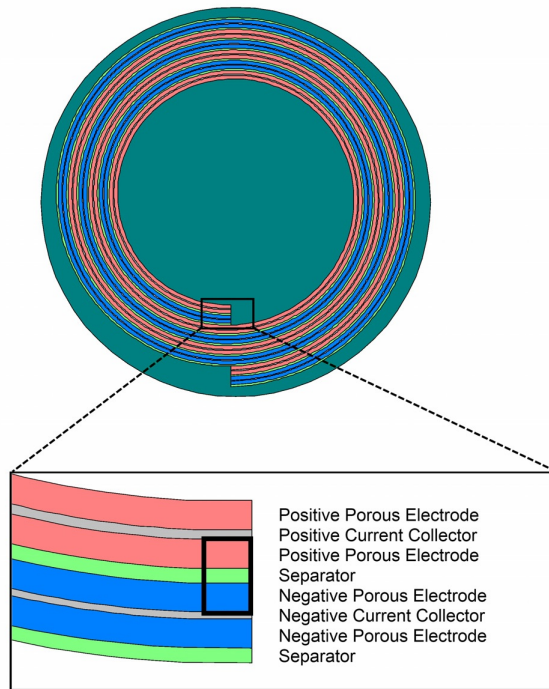


**Figure 3.1:** Spirally wound battery; the dark box indicates the simulated region [34]

The model consists of the two porous insertion electrodes (the anode on the left and the cathode on the right side), which are kept apart by a separator. The separator as well as the electrodes are filled with the organic liquid electrolyte. The electrodes are assumed to be superimposed continua of active electrode material, electrolyte and conductive additives, therefore at each point of the electrode, the solid phase as well as the liquid phase exists.

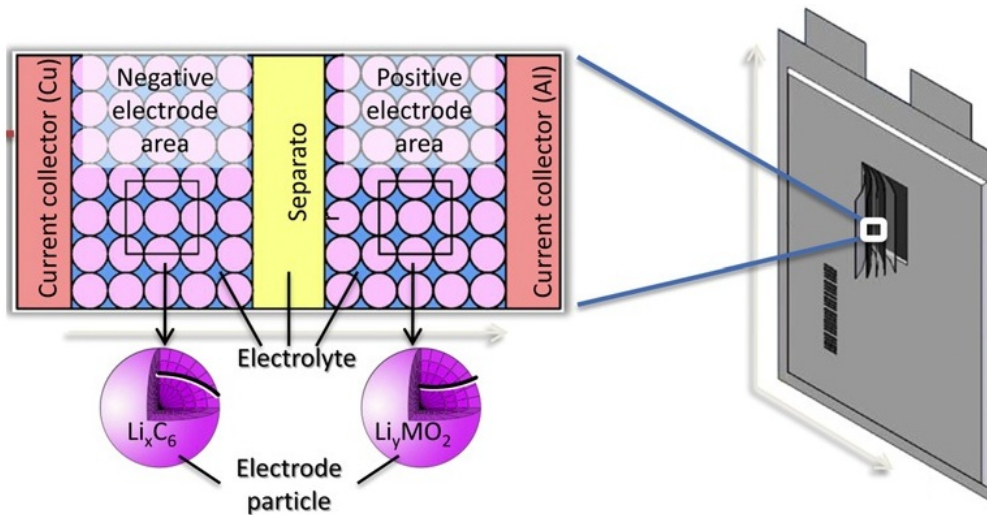


Figure 3.2: Pouch cell geometry [35]

### 3.2.2 Mesh elements

Two different meshes were used in the simulation software: a coarse mesh for the general model and a normal mesh to perform the parametric sweep (see figure 3.3).

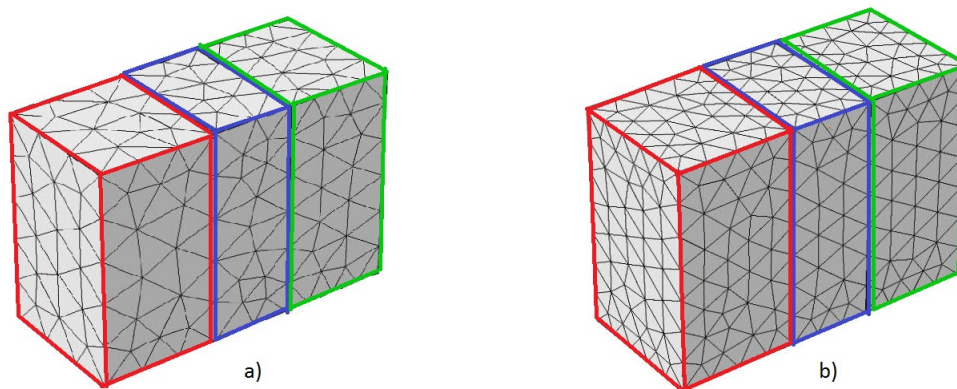


Figure 3.3: Different meshes of the simulated model; a...Coarse, b...Normal; red...Anode, blue...Separator, green...Cathode

## Coarse mesh

Both meshes consisted of tetrahedral elements. The coarse mesh contained 1515 elements and the number of degrees of freedom solved for was 2368. The parameters were:

**Table 3.1: Coarse mesh parameters**

Parameter	Value
Maximum element size	$3.42 \cdot 10^{-5}$ m
Minimum element size	$6.38 \cdot 10^{-6}$ m
Maximum element growth rate	1.6
Resolution of narrow regions	0.4

The mesh quality is time-invariant and only depends on the number of elements, the geometry of the model and the element shape. Therefore, the quality distribution and other statistics of the mesh elements were displayed immediately after the mesh creation (see figure 3.4).

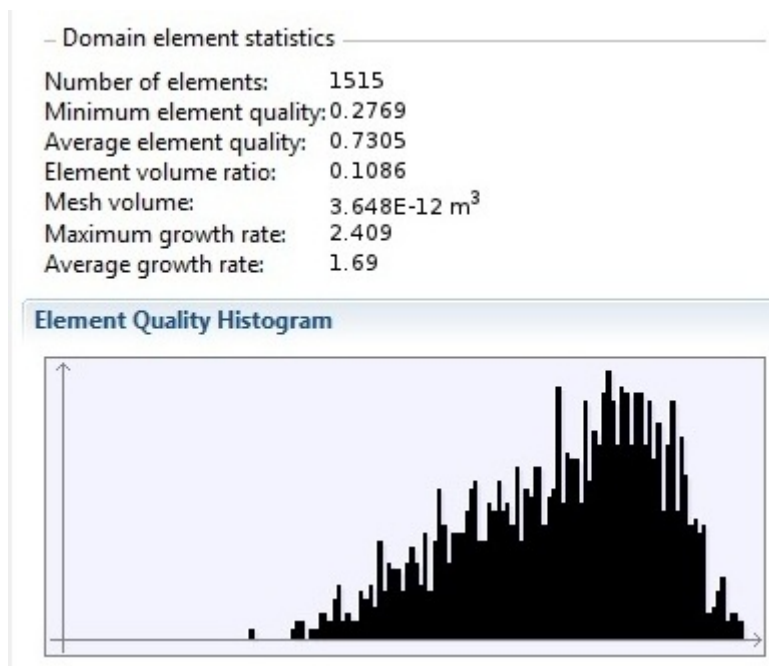


**Figure 3.4: Statistics of the coarse mesh element quality**

According to the mesh statistics, the average mesh element quality of the coarse mesh was 0.7305, the minimum element quality was 0.2769.

The quality of a mesh depends solely on the elements and does not rely on the equations solved for. It determines the accurateness of the results and therefore, the correlation between the reliability of the results and the quality of the mesh elements is very high [36].

Element qualities around 0.3 are poor, nevertheless, the minimum element quality, according to the distribution histogram, was an outlier. Most elements' qualities were higher and average values around 0.7 are good for a coarse mesh.

## Normal mesh

The normal mesh contained 4697 elements and the number of degrees of freedom solved for was 6629. The parameters for the normal mesh element size were:

**Table 3.2: Normal mesh parameters**

<b>Parameter</b>	<b>Value</b>
Maximum element size	$2.28 \cdot 10^{-5}$ m
Minimum element size	$4.1 \cdot 10^{-6}$ m
Maximum element growth rate	1.5
Resolution of narrow regions	0.5

The quality distribution of the normal mesh is quite similar to that from the coarse one (see figure 3.5).

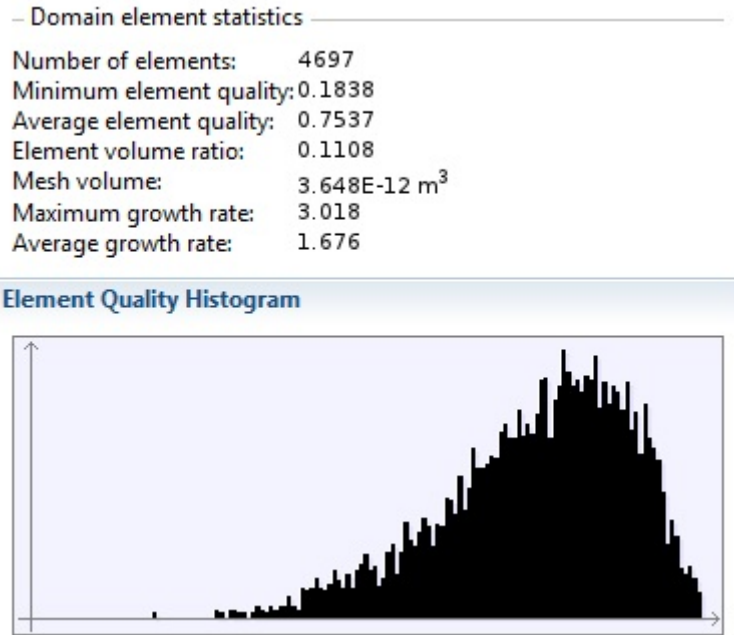


**Figure 3.5: Statistics of the normal mesh element quality**

The average mesh element quality of the normal element size was 0.7537, while the minimum element quality was 0.1838. As expected, the average element quality of the finer mesh is higher than the quality of the coarse mesh. The minimum element quality is lower, which is an outlier. Generally, the element qualities are acceptable high for the purposes.

Comparing different meshes for the same geometry demonstrates how the number of elements and, according to this, the number of degrees of freedom (which equals computation time) strongly rises with the element size. The element quality doesn't rise that much in comparison with

## 4 Mathematical description of battery processes

### 4.1 Electrolyte

#### 4.1.1 Mass transport and current distribution

The transfer of charged species in the electrolyte is described using the Nernst-Planck equation (transport caused by convection is neglected, bold letters are vectors) [37].

$$\mathbf{J}_{l,i} = -D_{l,i}\nabla c_{l,i} + \frac{z_i F}{RT} D_{l,i} c_{l,i} \mathbf{E}_l \quad (4.1)$$

The first term is the diffusion term and the second term considers migration. The Index  $i$  stands for  $\text{Li}^+$  or  $\text{PF}_6^-$  respectively, which are the two ionic species in the electrolyte.

$\mathbf{E}_l$  represents the electric field and is defined as

$$\mathbf{E}_l = -\nabla\varphi_l \quad (4.2)$$

The relation between the molar flux and the total current density is

$$\mathbf{j}_{l,i} = \sum_i \mathbf{J}_{l,i} z_i F \quad (4.3)$$

The diffusion current density is

$$\mathbf{j}_{l,d,i} = z_i F D_{l,i} \nabla c_{l,i} \quad (4.4)$$

And with the migration current density

$$\mathbf{j}_{l,m,i} = \frac{F^2 z_i^2}{RT} D_{l,i} c_{l,i} \mathbf{E}_l \quad (4.5)$$

The total current density is given by [37]

$$\mathbf{j}_l = F \sum_i z_i D_{l,i} \nabla c_{l,i} - \frac{F^2}{RT} \mathbf{E}_l \sum_i z_i^2 D_{l,i} c_{l,i} \quad (4.6)$$

The applied current at the current collector is the integral of the current density over the boundary

$$I_{app} = \int_{d\Omega} \mathbf{j} \cdot d\mathbf{s} \quad (4.7)$$

#### 4.1.2 Conservation laws

The variation of the species by time is directly related to the molar flux alteration by

$$\frac{\partial c_{l,i}}{\partial t} = -\nabla \cdot \mathbf{J}_{l,i} = D_{l,i} \nabla^2 c_{l,i} - \frac{z_i F}{RT} D_{l,i} \nabla c_{l,i} \nabla \cdot \mathbf{E}_l \quad (4.8)$$

At the electrodes, the flux of  $\text{Li}^+$  is connected to the current density via

$$\mathbf{n} \cdot \mathbf{J}_{\text{Li}^+} \big|_{x=L_a} = -\frac{I}{AF} \quad (4.9)$$

$$\mathbf{n} \cdot \mathbf{J}_{\text{Li}^+} \big|_{x=L_a+L_{sep}} = \frac{I}{AF} \quad (4.10)$$

and without  $\text{PF}_6^-$  flux variation

$$\mathbf{n} \cdot \mathbf{J}_{\text{PF}_6^-} \big|_{x=L_a} = 0 \quad (4.11)$$

$$\mathbf{n} \cdot \mathbf{J}_{\text{PF}_6^-} \big|_{x=L_a+L_{sep}} = 0 \quad (4.12)$$

Electroneutrality within the electrolyte is given by

$$\sum_i z_i c_i = 0 \quad (4.13)$$

Combining equation 4.13 and 4.8 leads to the concentration profile

$$\frac{\partial c_l}{\partial t} = \frac{2D_{\text{Li}^+} D_{\text{PF}_6^-}}{D_{\text{Li}^+} + D_{\text{PF}_6^-}} \nabla^2 c_l \quad (4.14)$$

With boundary conditions

$$\mathbf{n} \cdot \nabla c_l \big|_{x=0} = \mathbf{n} \cdot \nabla c_l \big|_{x=L_{tot}} = 0 \quad (4.15)$$

The electric field can be calculated using equation 4.8 and set the flux zero to derive [26]

$$\mathbf{E}_l = -\frac{\nabla c_l}{c_l} \frac{RT}{F} \quad (4.16)$$

And the boundary conditions are

$$-\mathbf{n} \cdot \mathbf{E}_l \Big|_{x=0} = -\mathbf{n} \cdot \mathbf{E}_l \Big|_{x=L_{tot}} = 0 \quad (4.17)$$

### 4.1.3 Electrolyte in the pores of the electrode

Caused by the fact, that the electrode regions consist of solid active particles and liquid electrolyte within the pores, these regions are calculated using the volume averaging technique derived by the porous electrode theory [5]. The material balance of the inserted species is calculated elsewhere (see equation 4.24).

The material balance of the electrolyte inside the pores is given by

$$\frac{\partial \epsilon_l c_l}{\partial t} = -\nabla \cdot \mathbf{J}_l \epsilon_l + r_l \quad (4.18)$$

The second term is the volume averaged flux density, given by 4.1.

The first term is the reaction rate and describes the production of lithium ions. The reaction is assumed to be of first order and is defined as

$$r_l = k_l \cdot c_l \quad (4.19)$$

The reaction rate constant is calculated by [38]

$$k_l = k_0 \cdot \exp \left[ -\alpha \frac{F}{RT} (U_x - U_{eq}) \right] \quad (4.20)$$

And for the backward reaction

$$k_l = k_0 \cdot \exp \left[ (1 - \alpha) \frac{F}{RT} (U_x - U_{eq}) \right] \quad (4.21)$$

$U_x$  is the local potential difference and defined as

$$U_x = \varphi_s - \varphi_l \quad (4.22)$$

While  $U_{eq}$  is the equilibrium potential difference and therefore

$$U_{eq} = \varphi_{eq,s} - \varphi_{eq,l} \quad (4.23)$$

## 4.2 Electrode particles

### 4.2.1 Mass transport

For the diffusion of intercalated lithium from the inner particle to the surface, Fick's second law is applied.

$$\frac{\partial c_s}{\partial t} = \nabla \cdot D_{Li} \nabla c_s = -\nabla \cdot \mathbf{J}_{Li} \quad (4.24)$$

Boundary conditions are

$$\mathbf{n} \cdot \nabla c_s |_{x=0} = \mathbf{n} \cdot \nabla c_s |_{x=L_{tot}} = 0 \quad (4.25)$$

If there is no side reaction at the electrode, the current is directly related with the flux of lithium ions at the electrode surface

$$-\mathbf{J}_{Li} |_{x=L_{sf}} = D_{Li} \nabla c_s |_{x=L_{sf}} = -\frac{I}{aFA} \quad (4.26)$$

And without flux at the current collector [39]

$$-\mathbf{J}_{Li} |_{x=0} = D_{Li} \nabla c_s |_{x=0} = 0 \quad (4.27)$$

The specific interfacial area is defined as (assuming spherical particles)

$$a = \frac{3\epsilon_s}{R} \quad (4.28)$$

### 4.2.2 Electrode potentials

The electrode potential can be calculated from the Nernst equation

$$\varphi_s = \varphi_{s,0} + \frac{RT}{F} \ln \frac{c_{Li^+}}{c_{Li}} \quad (4.29)$$

The equilibrium potential also varies with the concentration of the lithium inside the electrode particles and therefore should be interpolated with experimental data. The anode is assumed to be grounded

$$\varphi_a |_{x=0} = 0 \quad (4.30)$$

The equilibrium potential of the electrodes is a function of the state-of charge, which is defined as

$$SOC = \frac{C_s}{C_{s,max}} \tag{4.31}$$

The data for the equilibrium potentials are taken from the Comsol Model Library [40]. The functions are obtained by interpolation.

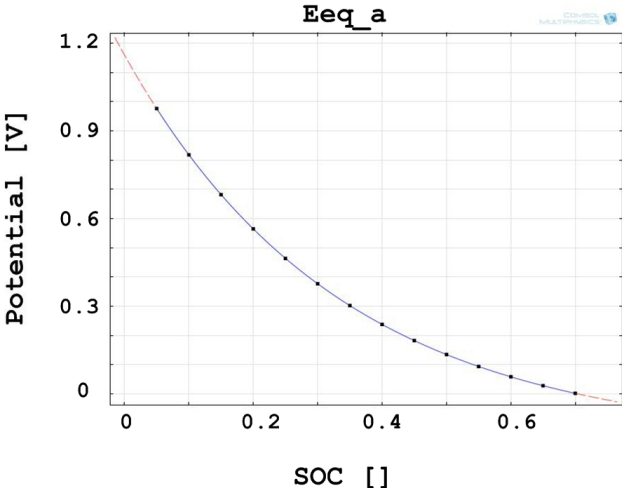


Figure 4.1: Equilibrium potential of the anode

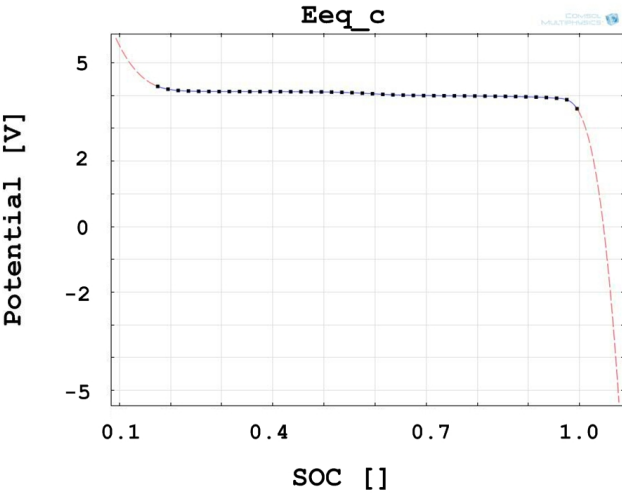


Figure 4.2: Equilibrium potential of the cathode

### 4.2.3 Charge conservation

Another form of Ohm's law is given by

$$\mathbf{j}_s = \sigma_s \nabla \varphi_s \quad (4.32)$$

The consequence of electroneutrality is

$$\nabla \cdot \mathbf{j}_s + \nabla \cdot \mathbf{j}_l = 0 \quad (4.33)$$

At the current collectors

$$-\sigma_a \nabla \varphi_a |_{x=0} = \sigma_c \nabla \varphi_c |_{x=L} = \frac{I}{A} \quad (4.34)$$

And without current at the separator [41]

$$\mathbf{n} \cdot \nabla \varphi_s |_{x=L_a} = \mathbf{n} \cdot \nabla \varphi_s |_{x=L_a+L_{sep}} = 0 \quad (4.35)$$

# 5 Implementation in COMSOL Multiphysics

## 5.1 The COMSOL environment

The COMSOL environment consists of the *Model builder*, the *Node settings* and the *Graphics* window (see figure 5.1).

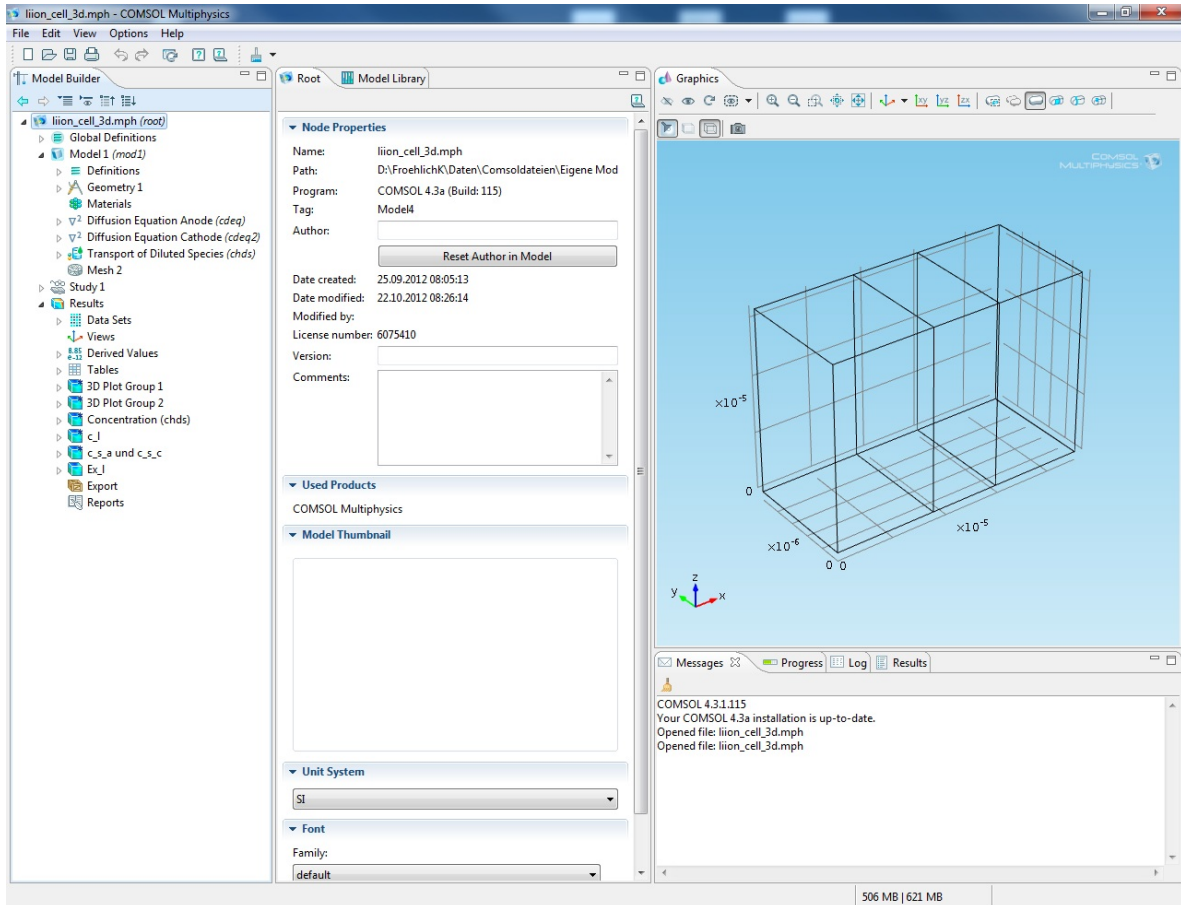


Figure 5.1: COMSOL desktop of the electrochemical model

The *Model builder* window is the main section of the program. It contains all details of the model: global definitions, physics, studies and results. If one branch in the *Model builder* window is marked, the related information is presented in the *Node settings* window and corresponding settings can be modified. The *Graphics* window displays the present domains of the model and where the physics are applied to. The results are also plotted in this window.

The root node in the *Model builder* window is structured into four main branches: *Global definitions*, *Model*, *Study* and *Results*. The branches also contain several subdivisions and feature nodes. It is possible to add diverse models and studies into one project file to compare the results, in this example, only one model and one study were applied.

### 5.1.1 Global definitions

The *Global definitions* branch contains global parameters, variables and functions. Values defined within this branch are applied to the whole model. Parameters and variables can be loaded from an and saved to a Microsoft Excel or Editor file.

### 5.1.2 Model

The *Model* branch comprises *Definitions*, *Geometry*, *Materials*, *Physics interfaces* and the *Mesh*.

In the *Definitions* branch, one can define local variables, functions, probes, model couplings, selections, pairs and coordinate systems. The model introduced here, used local variables and model couplings (integration over a domain/boundary). The variables can be defined on particular domains, boundaries or the whole model.

Within the *Geometry* branch, one can choose between different geometric structures to build the model. Blocks, cones, cylinders, spheres and other primitives are predetermined and, using Boolean operations differences, unions and intersections of the devices can be built. *Form a union* is the default finalization method, *Form an assembly* is another option. The difference is the validity of the condition of continuity.

Materials can be added to the domains of the model within the *Materials* branch. Materials can be chosen from a library or defined apart. The properties of the added materials can be used within the *Physics interfaces*, for example the conductivity or diffusion coefficient. In this model, no material was defined and the parameters were derived from the predefined parameter list under *Global Definitions*.

The next branches are the so-called *Physics interfaces*. *Physics interfaces* are templates with predefined variables and equations covering different physics areas [42]. Each interface consists of default domain and boundary features, other nodes can also be added using the context menu when right-clicking the interface icon (see figure 5.2).

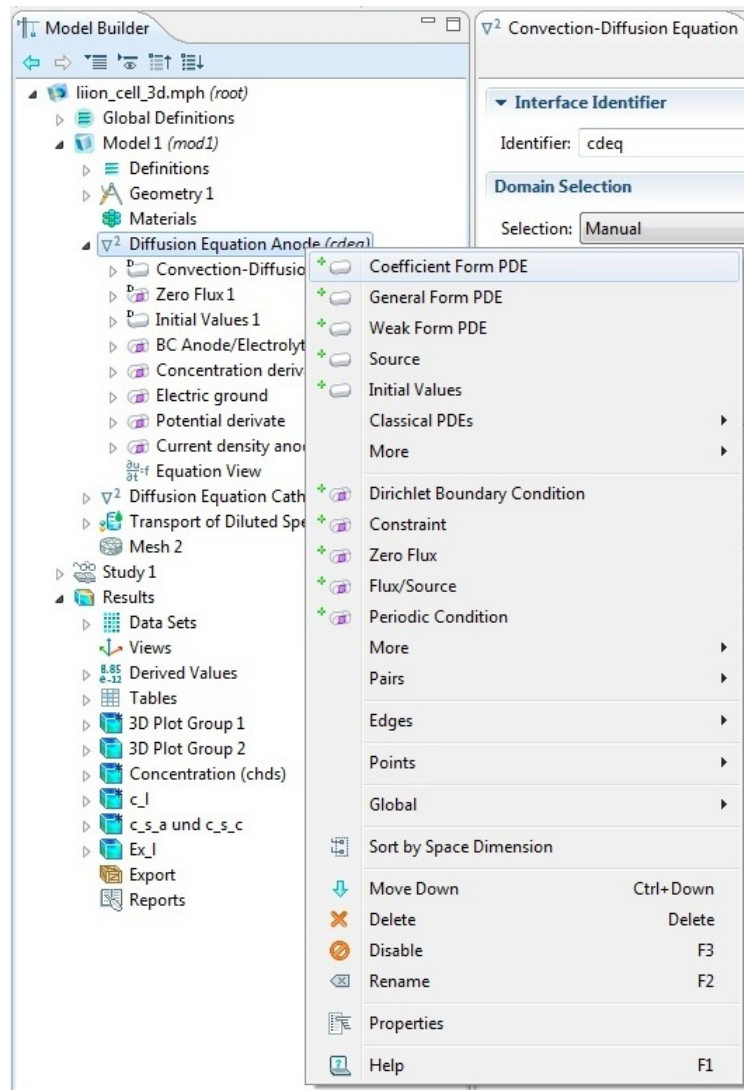
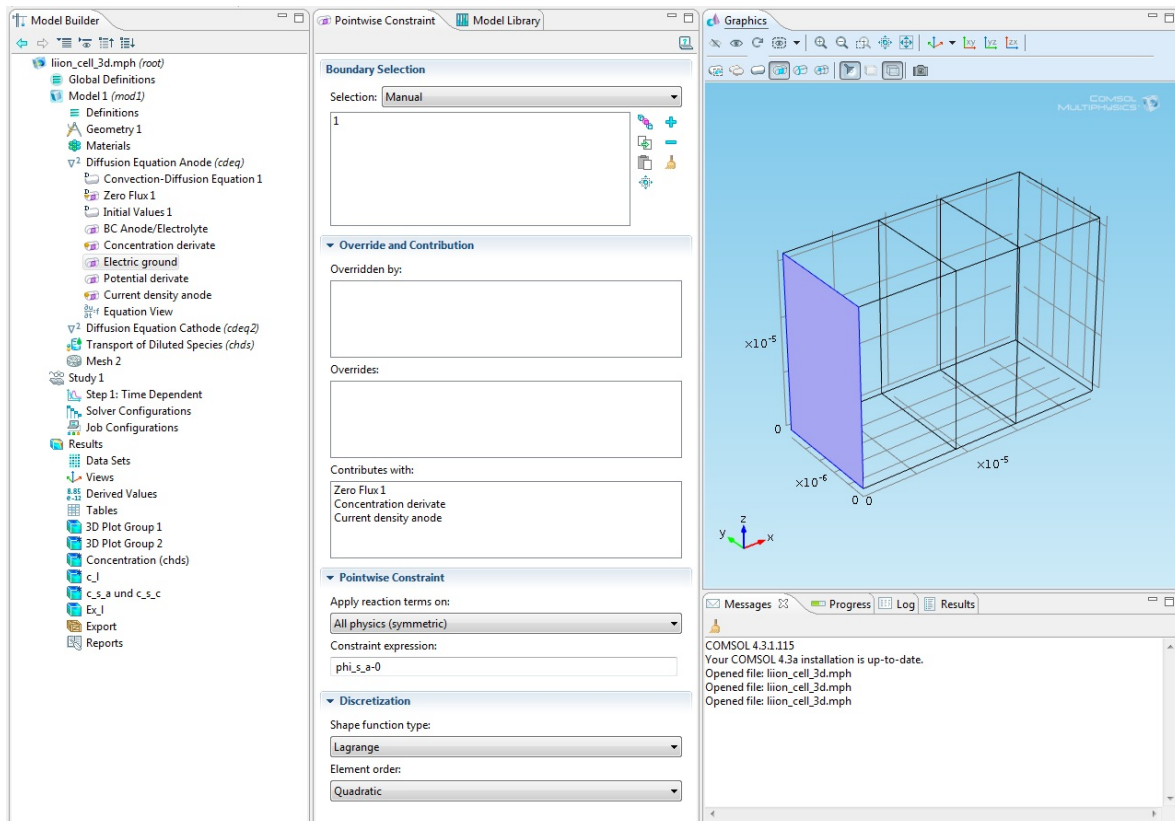


Figure 5.2: Feature nodes of the *Convection-Diffusion Equation* interface

The default feature nodes are marked with a *D* on the left side, other nodes were added separately. The clear features are domain conditions while those with the purple margin symbolize boundary conditions. When a feature node is added, the area of validity has to be chosen. The *Contribution* section displays how the feature contributes with or overrides other features. On the next section, the equation or parameters are inserted and on the last section, *Discretization*, the shape function type and its element order can be changed (see figure 5.3).



**Figure 5.3: Example for a feature node, its settings and boundary selection (*Electric ground - Pointwise Constraint*)**

The *Mesh* branch divides the geometry model into small (mesh) elements. Tetrahedral elements are the default setting, but hexahedral, prism or pyramid elements do also exist. After choosing the geometry of the elements, the next step is to define the size of the elements. The predefined sizes reach from extremely coarse to extremely fine. If the desired size differs from the predefined ones, the element size parameters can be changed in the *Node settings* window. Additionally, more *Mesh* branches can be added, to compare the results between different mesh types and/or sizes.

### 5.1.3 Study

The first node under the *Study* branch is the chosen study type; in this case: *Time Dependent*. It can be useful to add additional study steps, for example if the time-dependent solver does not converge, it is helpful to solve the model stationary first. Within the study step node, study settings like tolerances, physics and mesh selections, and, in this model, the time range can be varied.

The next node is the *Solver Configurations* icon. An independent solver for each study step is generated within this branch. Between the solver, it is necessary to add a *Store Solution* feature so that the solution from the preceding solver can be used as initial values for the next solver. Within the *Time-Dependent Solver* node, settings like absolute tolerance, results while solving, output, time stepping and method of time stepping, and others are displayed.

#### 5.1.4 Results

The *Results* branch provides data sets, derived values and tables. The visualization and evaluation of the results are stored when the model is solved. 3D Plots, Surface Plots, Graph Plots and others can be added to visualize the derived dependent variables.

## 5.2 Building a model

### 5.2.1 Model Wizard

When the COMSOL Multiphysics program was started, the so-called *Model Wizard*, a supporting tool, was shown in the *Node settings* window. The first selection was the space dimension of the electrochemical model. The model is three-dimensional, so 3D was selected. The next step, according to the wizard, was to add physics. The interfaces are sorted by their physical properties. In the introduced model, two *Convection-Diffusion Equation* interfaces, belonging to *Mathematics/Classical PDEs*, and one *Transport of Diluted Species* interface, belonging to *Chemical Species Transport*, were added. The physics interfaces were added by clicking *Add Selected* and the names of the dependent variables were changed within the settings window. After that, the study type was selected. The preset studies for the selected physics were *Stationary* or *Time-dependent*. The *Time-Dependent* study was chosen here. By clicking the *Finish* button, the *Model Wizard* window closed and the *Model Builder* window expanded the *Model* branch containing the chosen interfaces and belonging default features (see figure 5.4).

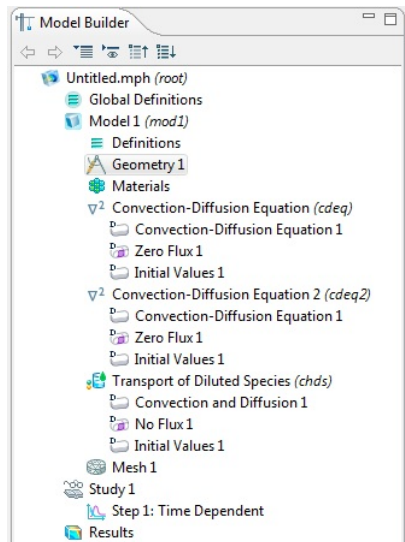


Figure 5.4: Default view of the model builder window

## 5.2.2 Geometry

The next step was to build the geometry. This model has a simple geometry, consisting of three blocks. One by one, the blocks were added via right-clicking geometry and choosing block. In the node setting window, the size and position of the blocks were defined. The width, depth and height of the blocks were saved at *Global Definitions/Parameters* (see figure 5.5).

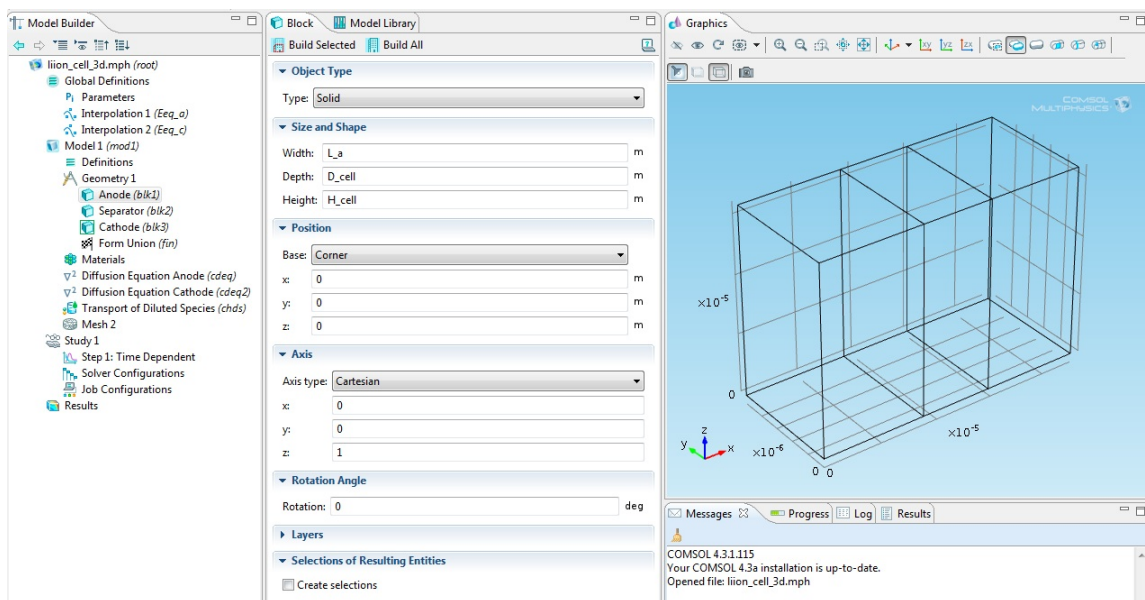


Figure 5.5: Geometry settings window

### 5.2.3 Variables, parameters and other definitions

As mentioned above, the parameters were saved in the *Global Definitions* branch. Variables were defined in the *Model/Definitions* node and, depending on which variables were defined, the corresponding domain was selected. Integration over boundaries were needed in this model, and could also be added by selecting *Model Couplings/Integration*. An integration operator over a chosen domain/boundary was established and could be used within the interfaces.

The equilibrium potentials as functions of the state-of-charge were derived by interpolation of the data from the Model library [40]. The interpolation was performed by loading the data from the file, setting the interpolation, name and the units of the function and plot it in the *Graphics* window (see figure 5.6).

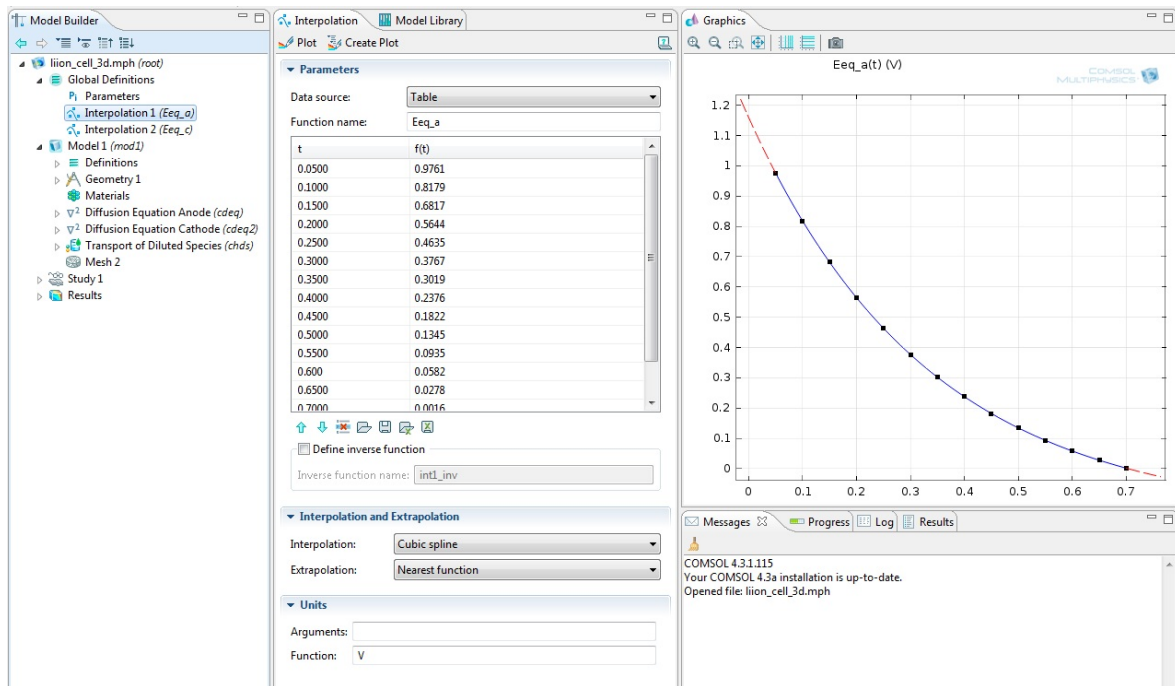


Figure 5.6: Interpolation of the data to define the anode potential function

## 5.2.4 Physics interfaces

Various steps were taken to completely define the physics of the model of the lithium ion cell. For the *Convection-Diffusion Equation* interface, the units of the dependent variable (concentration [ $\text{molm}^{-3}$ ]) and the source term (molar flux [ $\text{molm}^{-2}\text{s}^{-1}$ ]) had to be chosen and the valid domain was selected (anode/cathode). In the *Transport of Diluted Species* interface, the units were fixed, but the convective transport mechanism had to be deselected.

In the *Convection-Diffusion Equation* feature, the equation was displayed and the corresponding parameters were inserted in the *Node settings* window (see figure 5.7).

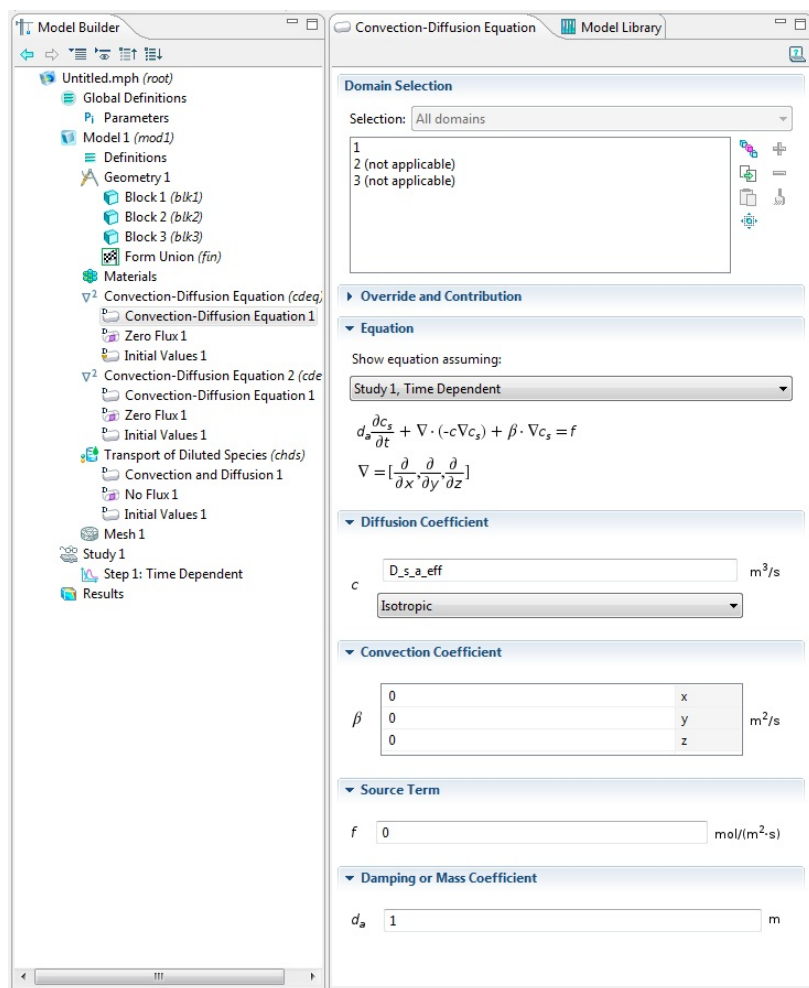


Figure 5.7: Settings of the *Convection-Diffusion Equation* feature node

Fluxes, boundary conditions and other features were added to the interfaces, until the model was fully defined and all concerning equations were added. In total, the electrochemical model consists of 49 nodes (boundary and domain features), the features are particularly listed in the appendix.

### 5.2.5 Meshing

The mesh was chosen by selecting *Free Tetrahedral* from the context menu. Two new nodes were created - *Size* and *Free Tetrahedral 1*. In the *Size* node, the size of the elements and the element parameters were chosen (see tables 3.2 and 3.1 on page 22). In the *Free Tetrahedral 1* node, the geometric entity level, scale geometry and control entities were selected. Finally, by pressing the button *Build Selected*, the mesh elements were created.

### 5.2.6 Study

In the *Study* node, because the model has not been computed yet, was only one feature node: *Step 1: Time Dependent*. The settings for the study was the time range and the tolerance of the model. The study step solved for all physics and no other study step was added. The chosen time was in a short range, in order to reduce computation time, in addition it is possible to interpolate the data to a longer time frame.

### 5.2.7 Parametric sweep

A sensitivity analysis was performed using the *Parametric sweep* feature. The node was added via the context menu of the study node. The settings for the *Parametric sweep* contain the parameter names and the value list (see figure 5.8). All combinations were chosen for the sweep type. The selected parameters were length (anode, cathode, separator), particle radii (anode, cathode) and volume fractions (solid and liquid phase anode/cathode).

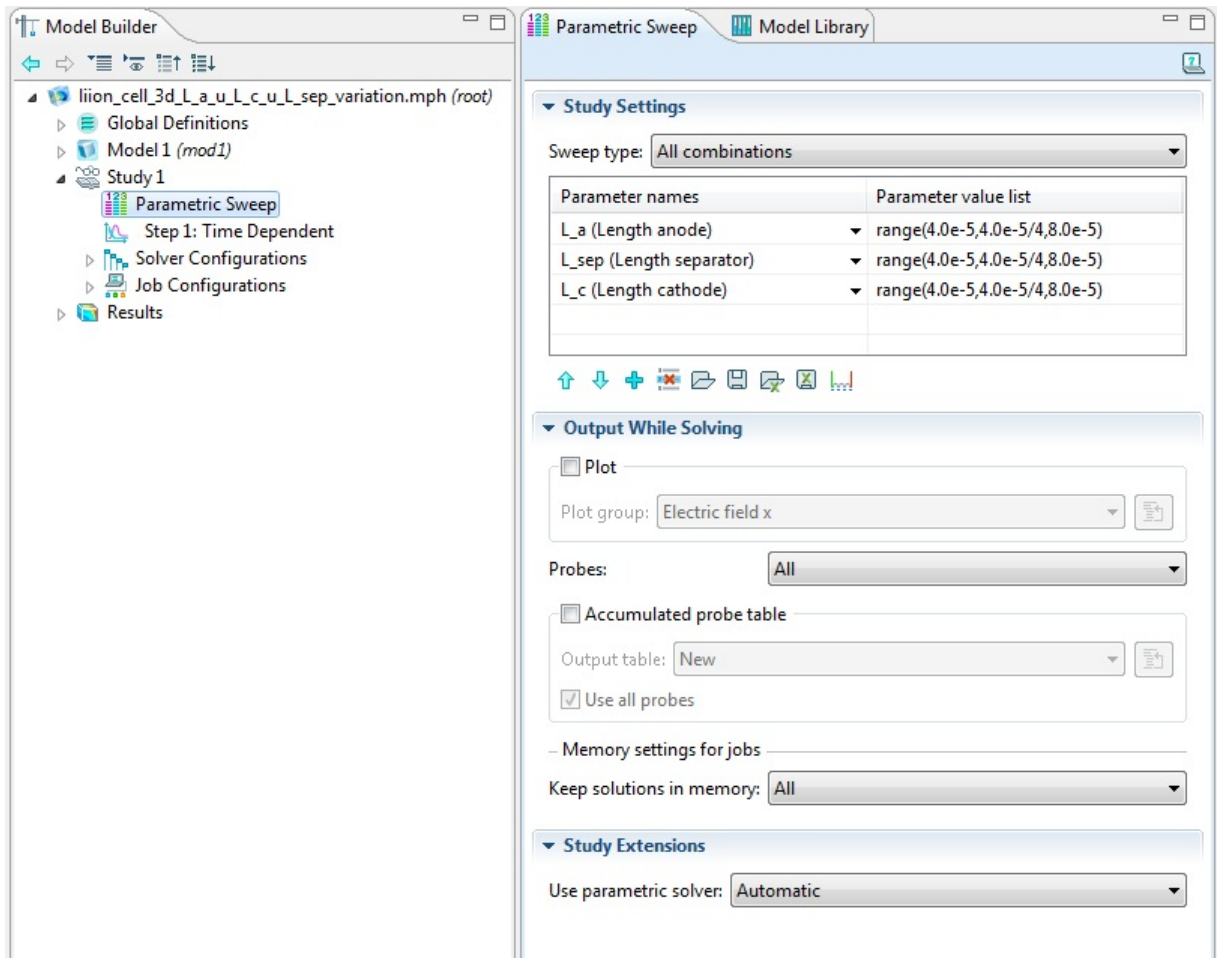


Figure 5.8: Settings of the *Parametric Sweep* node

## 6 Results and discussion

### 6.1 3D General model

The presented simulations were calculated with applied 10 s of charging at  $10 \text{ A m}^{-2}$  current density, which equals a current of  $1.6 \cdot 10^{-7} \text{ A}$  for the introduced model geometry.

#### 6.1.1 Lithium concentration in the solid phase

The lithium concentration in the solid phase was calculated and illustrated after 10 s of charging (see figure 6.1).

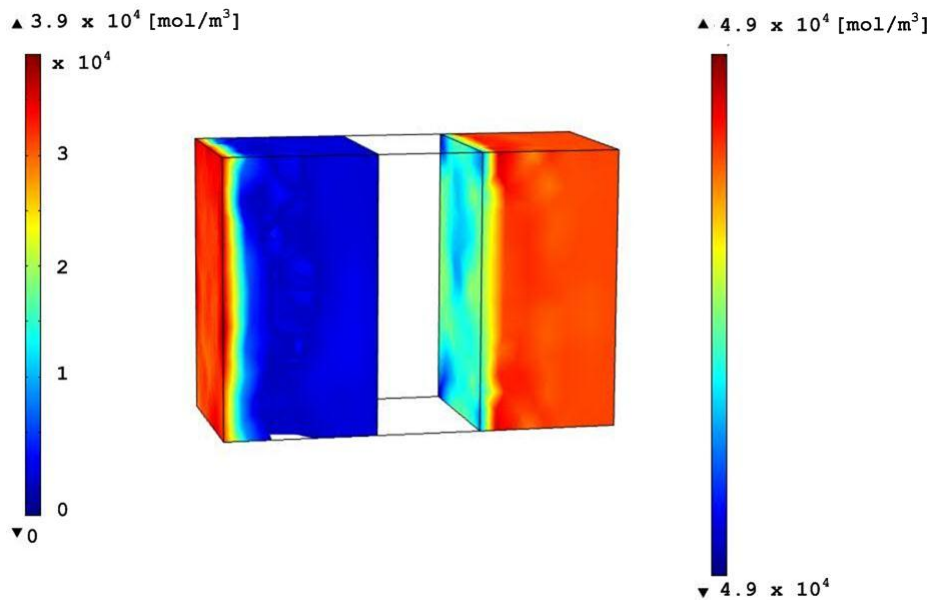
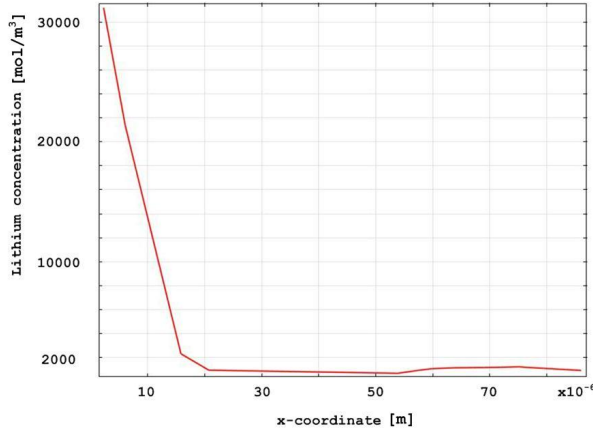


Figure 6.1: Lithium concentration in the solid phase of the electrodes

As mentioned before, during the charging process, the lithium is de-intercalated from the cathode (right side) and intercalated into the anode (left side). Therefore, the lithium concentration in the solid phase of the anode increased, while the concentration of the cathode decreased.

The concentration varied much more in the anode than in the cathode. The reason for this phenomenon is that the anode was assumed to be grounded and therefore the electric potential was set to zero at the current collector. The lithium concentration at the boundary facing the collector is very high, the influence of the electric ground reaches until the x-coordinate  $20 \cdot 10^{-6} \text{m}$  (see figure 6.2).



**Figure 6.2: Lithium concentration in the solid phase of the anode**

*In situ* measurements have shown, that the lithium is primarily intercalated and de-intercalated at the side of the electrode, which is facing the separator. Depending on the duration and current density of the charging or discharging process, the lithiation front is moving into the direction of the current collector [25]. This effect was observable on both electrodes, but easier to distinguish on the cathode side, due to smaller concentration variations. After 10 s of charging, some amount of lithium has been de-intercalated from the cathode and intercalated into the anode (see figure 6.3).

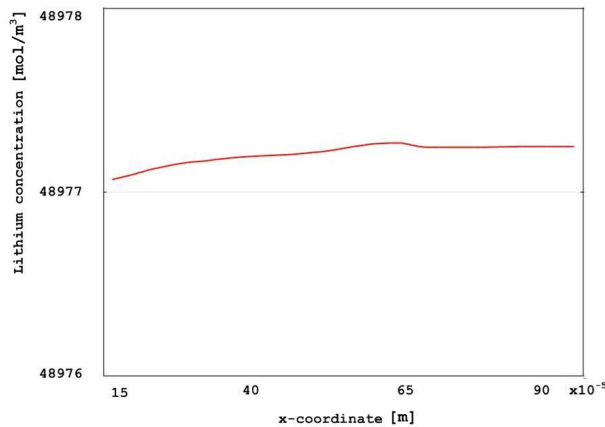


**Figure 6.3: Lithium concentration in the solid phase of the cathode**

### 6.1.2 Lithium concentration in the liquid phase

The lithium ion concentration changed intensely, even within the first seconds of charging (see figure 6.4).

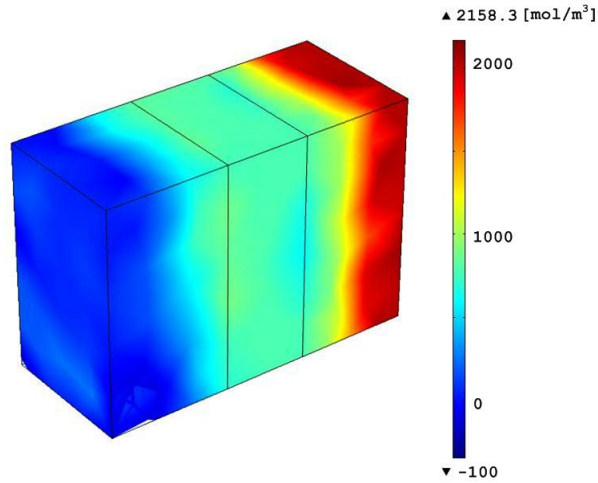


Figure 6.4: Lithium ion concentration in the electrolyte

The concentration was high at the positive electrode, and low at the negative electrode. The reason is that the lithium ions at the anode side react at the surface of the electrode and are intercalated into the graphite, while at the cathode side the lithium is deintercalated and lithium ions are produced (see figure 6.5).

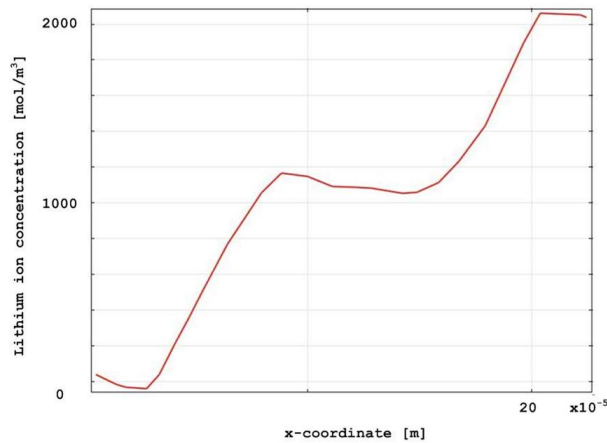


Figure 6.5: Lithium ion concentration in the electrolyte, x-axis

The slightly negative values at the anode side are caused by the time interpolation and the coarse mesh.

### 6.1.3 Lithium ion flux

The lithium ion flux in the electrolyte, as a vector, was solved individually for each coordinate (x,y,z). The flux was defined separately for each domain, which is the reason for the rather rough transitions at the inner boundaries (see figure 6.6).

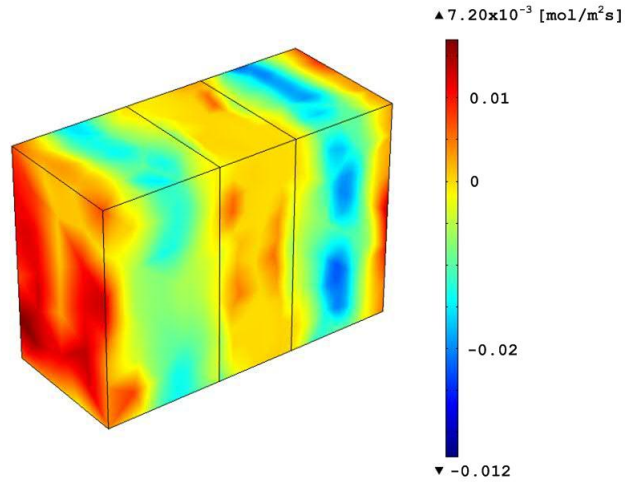


Figure 6.6: Lithium ion flux, x-coordinate

The lithium ion flux in the liquid phase is low at the inner side of the electrodes and high at the boundaries. Due to lower resistances at the separator region, the lithium ion flux rises at the inner side of the electrodes. In particular the x-coordinate of the vector displayed this phenomenon (see figure 6.7).

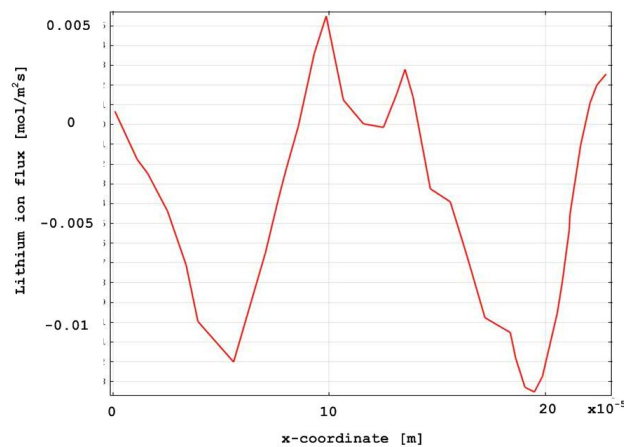


Figure 6.7: Lithium ion flux, x-axis

## 6.2 Particle radii variation

The particle radii of the solid phase of the anode and the cathode were varied between  $10^{-5}$  and  $10^{-7}$  m. The porosities of the electrodes were kept constant. The specific interfacial area, due to its definition (see equation 4.28 on page 28), was varied as well.

In a real cell, a particle size variation is mostly connected with a variation of the porosity. For bigger particles, the pores in the electrode increase and influence the performance of the cell. In this model, the influence of both parameters - porosity and particle radius - have been evaluated separately. The particle size has been changed without influencing transport properties of the lithium ions in the electrolyte in the pores of the electrodes.

Generally, the influence of the particle radius, compared to other parameters of the model, was quite low. Even if the size range was wide, the effect on the lithium-ion cell model was little. Instead of the full spatial scheme, mostly the one-dimensional graph is pictured for better readability.

### 6.2.1 Lithium concentration in the solid phase

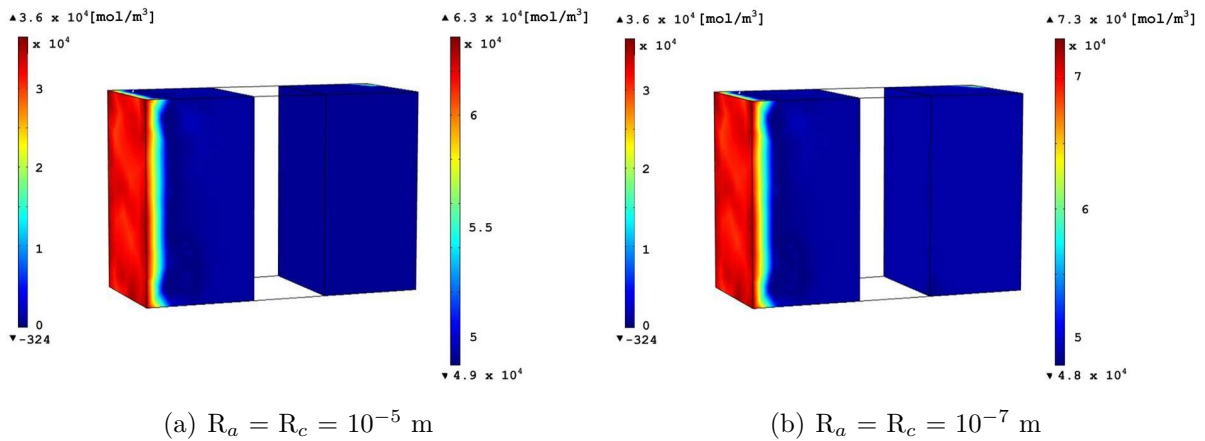


**Figure 6.8: Lithium concentration in the solid phase of the electrodes for different particle sizes**

In this model, according to the equations, the particle radii preferentially influenced the flux of lithium ions at the electrodes surfaces (see equation 4.26 on page 28).

Larger particle sizes led to a smaller specific interfacial area and therefore, a greater flux of lithium at the electrode surface and vice versa. Therefore, the lithium concentration in the solid phase of the electrodes varied more for the larger particle sizes than for the smaller ones (see figure 6.8 and 6.9).

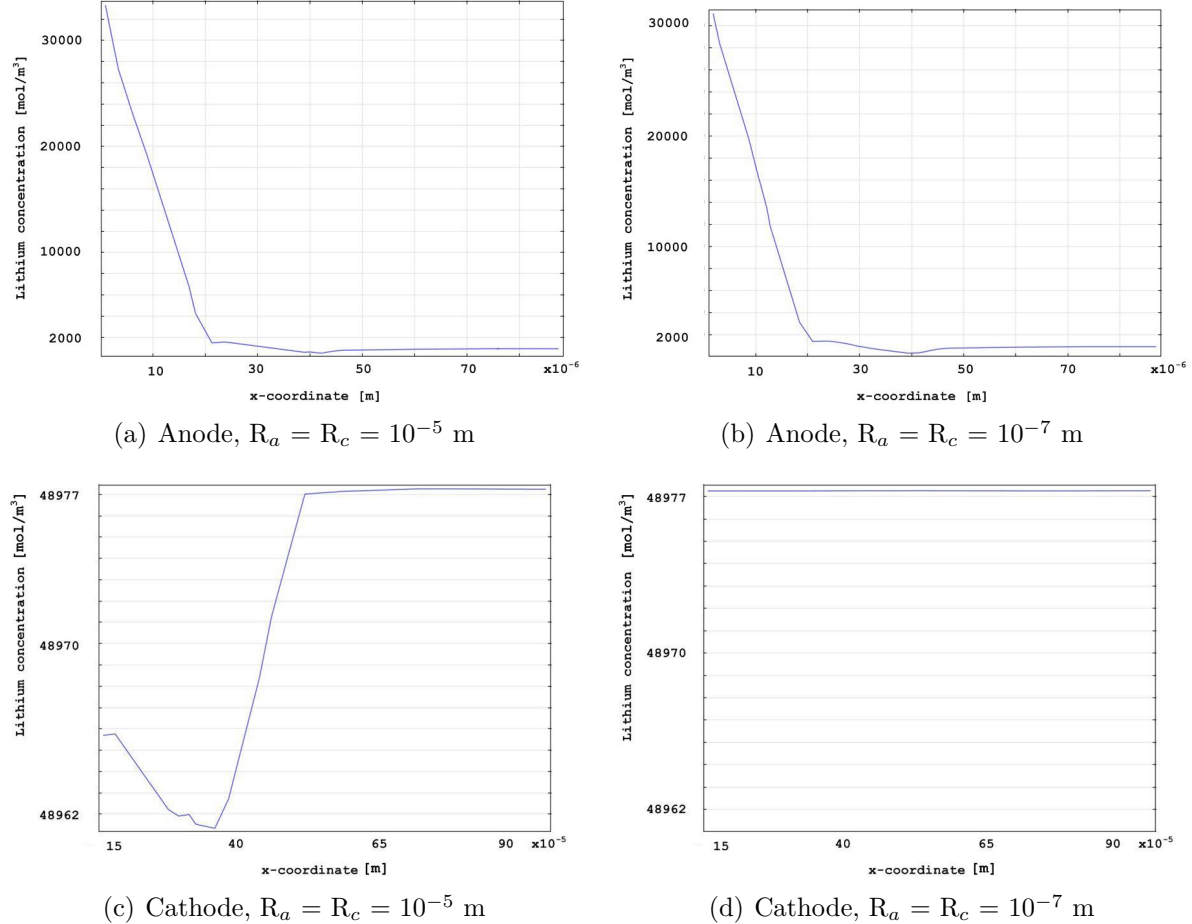


**Figure 6.9: Lithium concentration in the solid phase for different particle sizes, x-axis**

## 6.2.2 Lithium concentration in the liquid phase

The lithium ion concentration in the electrolyte didn't vary for different particle sizes. The slight discrepancies between of the values in the different particle sizes were natural oscillations and not classifiable as significant changes.

## 6.2.3 Lithium ion flux

As mentioned before, the particle size basically influenced the lithium flux at the boundary between the particle surface and the electrolyte. The lithium ion flux had higher values for the bigger particle sizes and lower values for the small particles (see figure 6.10).

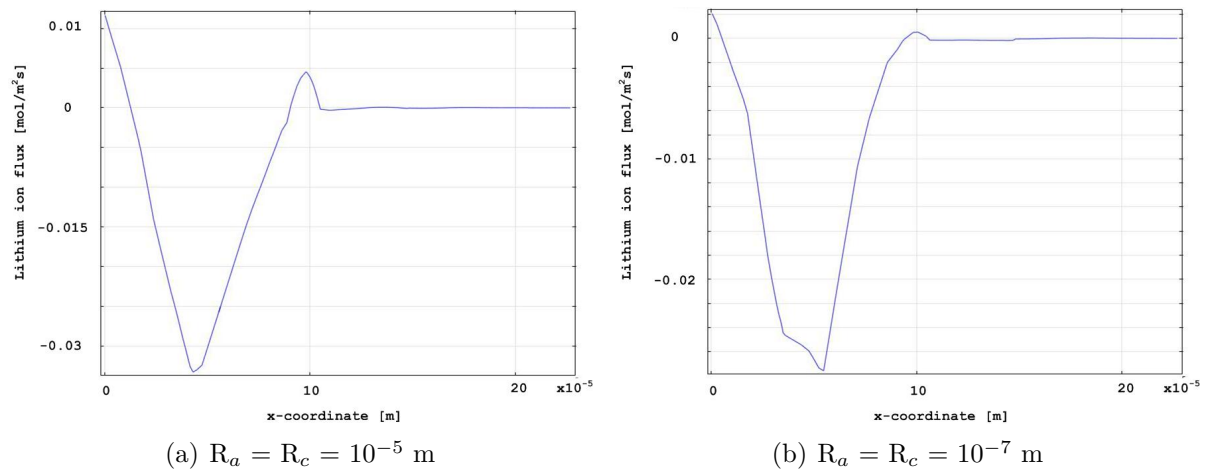


Figure 6.10: Lithium ion flux, x-axis

### 6.3 Volume fraction variation

The volume fractions of the solid phases of the electrodes were varied between 30 % and 60 % (anode), and between 40 % and 70 % (cathode). It was assumed, that the binder material was constant at 2.5 % (anode) and 4.5 % (cathode). This was achieved by defining the volume fractions of the liquid phase as following:

$$\epsilon_l = 1 - \epsilon_s - \epsilon_b \quad (6.1)$$

As mentioned before, volume averaging was performed in the electrodes. This means, the porous electrodes were treated as superimposed continua of both phases, the solid particles and the liquid electrolyte. This is performed by multiplying the transport property terms by the volume fraction to a correction factor, which is called *Bruggemann correction* [5].

The effective diffusion coefficients were calculated via

$$D_{eff} = D \cdot \epsilon^{brugg} \quad (6.2)$$

The effective conductivity of the phases were derived analog

$$\sigma_{eff} = \sigma \cdot \epsilon^{brugg} \quad (6.3)$$

The impact of the volume fractions on this electrochemical model was observed by these equations. When the volume fraction of the solid phase increased, the effective diffusion coefficient and the effective conductivity of the particles rose.

Additionally, when the volume fraction of the solid phase increased, the volume fraction of the liquid phase decreased and the effective diffusion coefficient for the electrolyte in the pores as well.

### 6.3.1 Lithium concentration in the solid phase

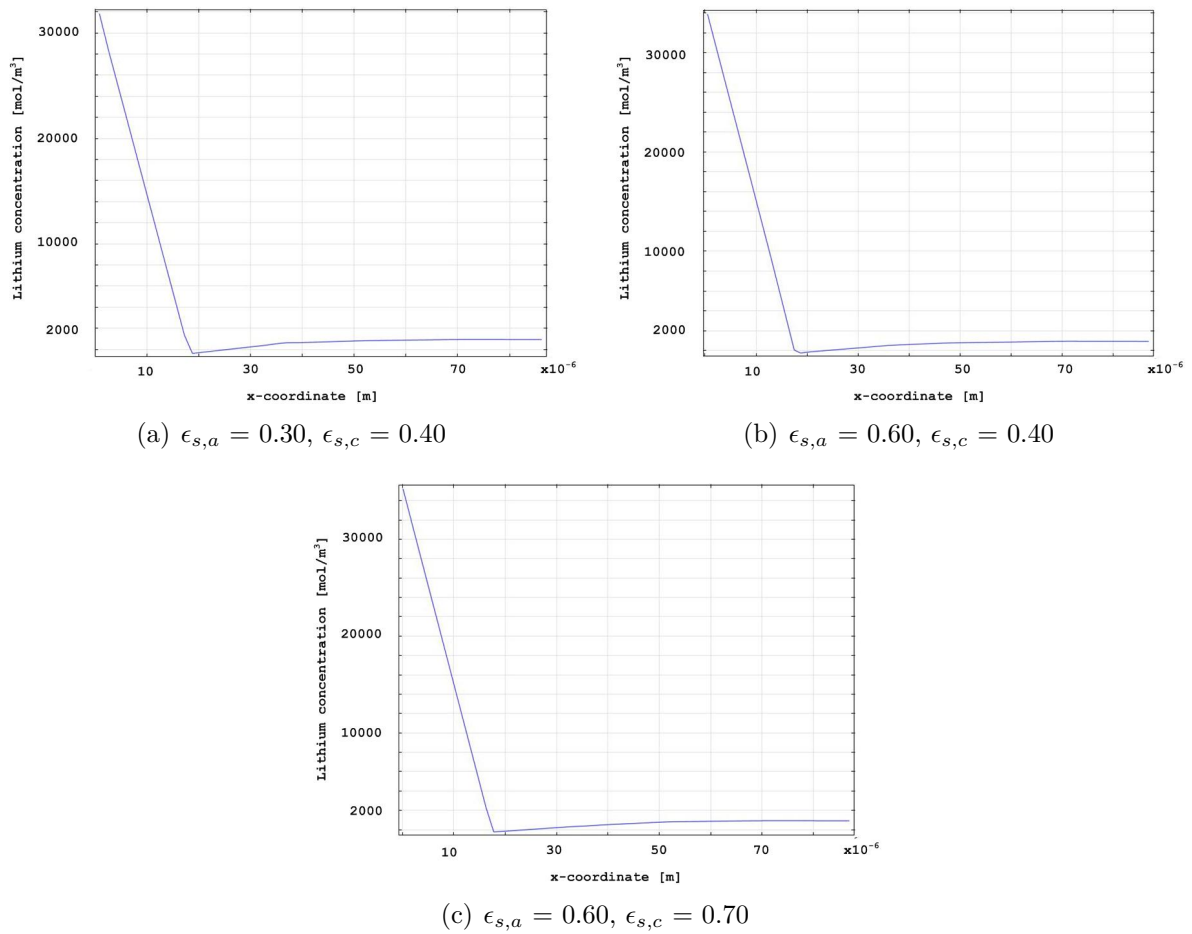
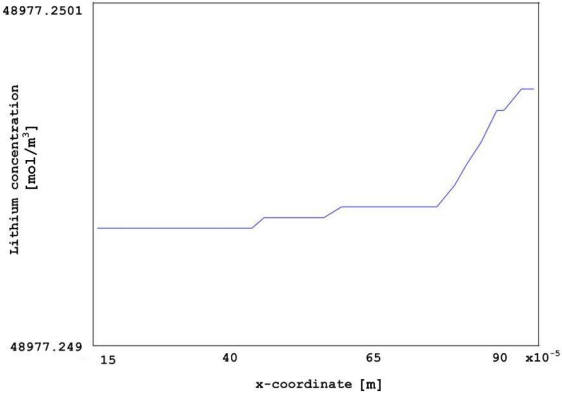


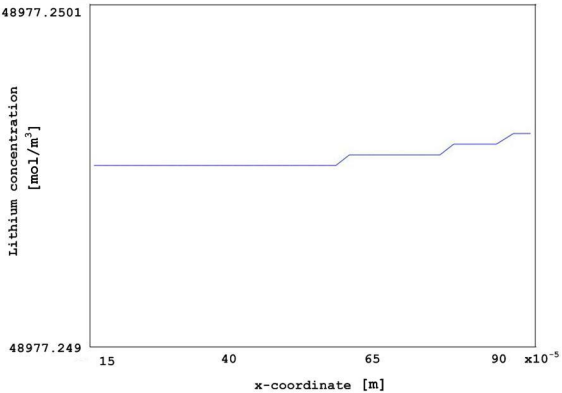
**Figure 6.11: Lithium concentration in the solid phase of the anode for different volume fractions, x-axis**

The concentration varied slightly in the electrodes (see figure 6.11). As mentioned above, the effective diffusion coefficient in the solid phase of the electrodes increased/decreased with the volume fraction. The lithium flux in the solid phase rose with its diffusion coefficient and therefore, the intercalation process was faster. But on the other hand, the flux of the lithium ions in the liquid phase decreased and the ionic transport in the electrode was inhibited.

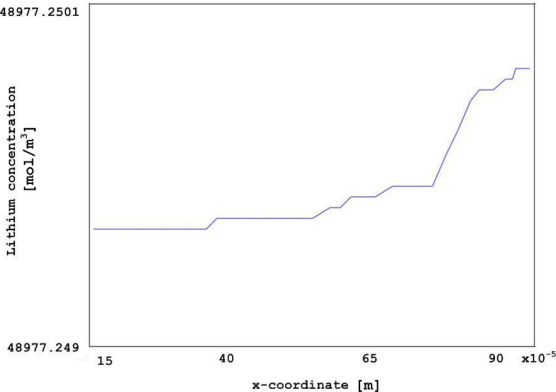
Therefore, the lithium concentration in the solid phases of the electrodes didn't differ much from each other (see figure 6.12).



(a)  $\epsilon_{s,a} = 0.30, \epsilon_{s,c} = 0.40$



(b)  $\epsilon_{s,a} = 0.60, \epsilon_{s,c} = 0.40$



(c)  $\epsilon_{s,a} = 0.60, \epsilon_{s,c} = 0.70$

**Figure 6.12: Lithium concentration in the solid phase of the cathode for different volume fractions, x-axis**

### 6.3.2 Lithium concentration in the liquid phase

The concentration of lithium ions in the electrolyte was similarly affected by the variation of the volume fraction than the concentration in the solid phase (see figure 6.13).

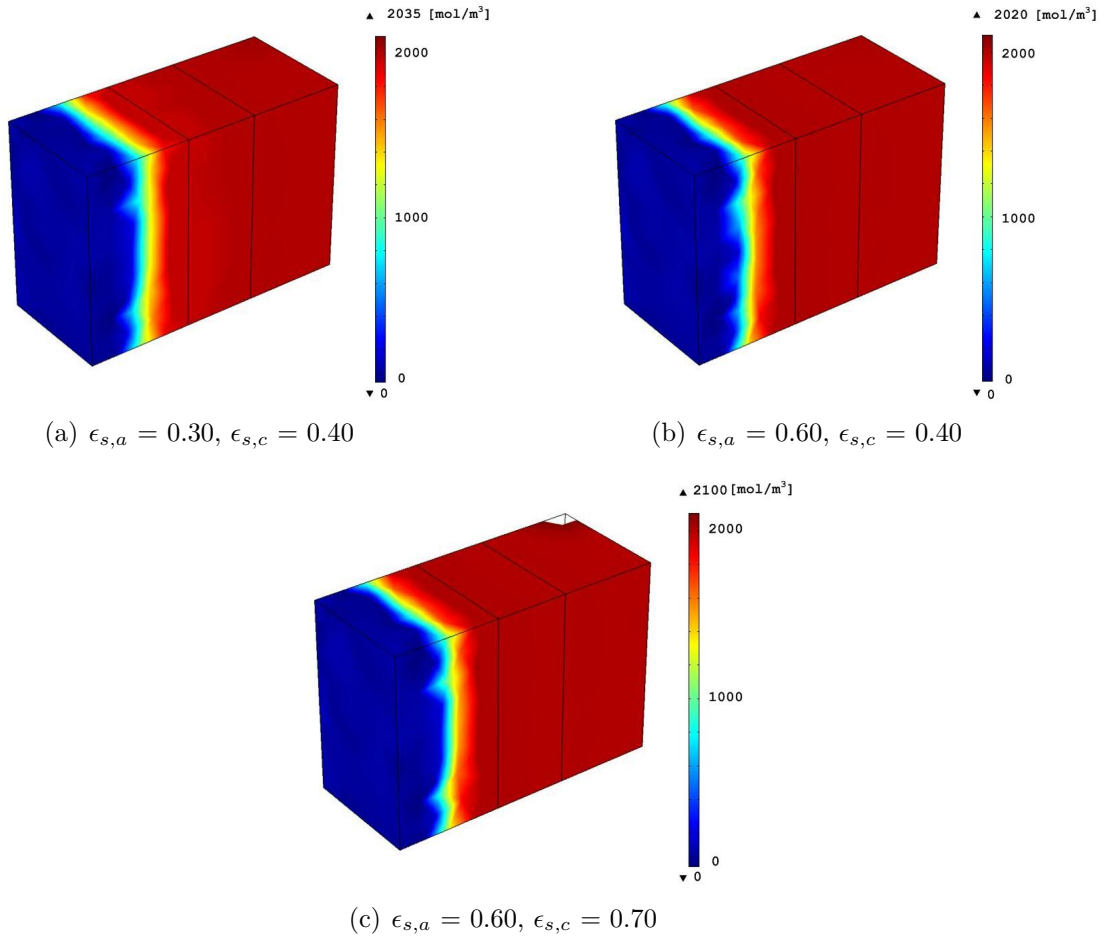


**Figure 6.13: Lithium ion concentration in the electrolyte for different volume fractions**

The border between the higher and the lower concentration was sharper for the greater volume fractions of the solid phases. This was caused by the lower diffusion coefficient in the electrolyte and smaller pores in the electrodes.

The missing edge at the current collector side of the cathode symbolizes a defect mesh element.

### 6.3.3 Lithium ion flux

The lithium ion flux, per definition, is straight proportional to the diffusion coefficient of the ions in the electrolyte. Apart from the separator region, the diffusion coefficient was replaced by the effective diffusion coefficient (see equation 6.2).

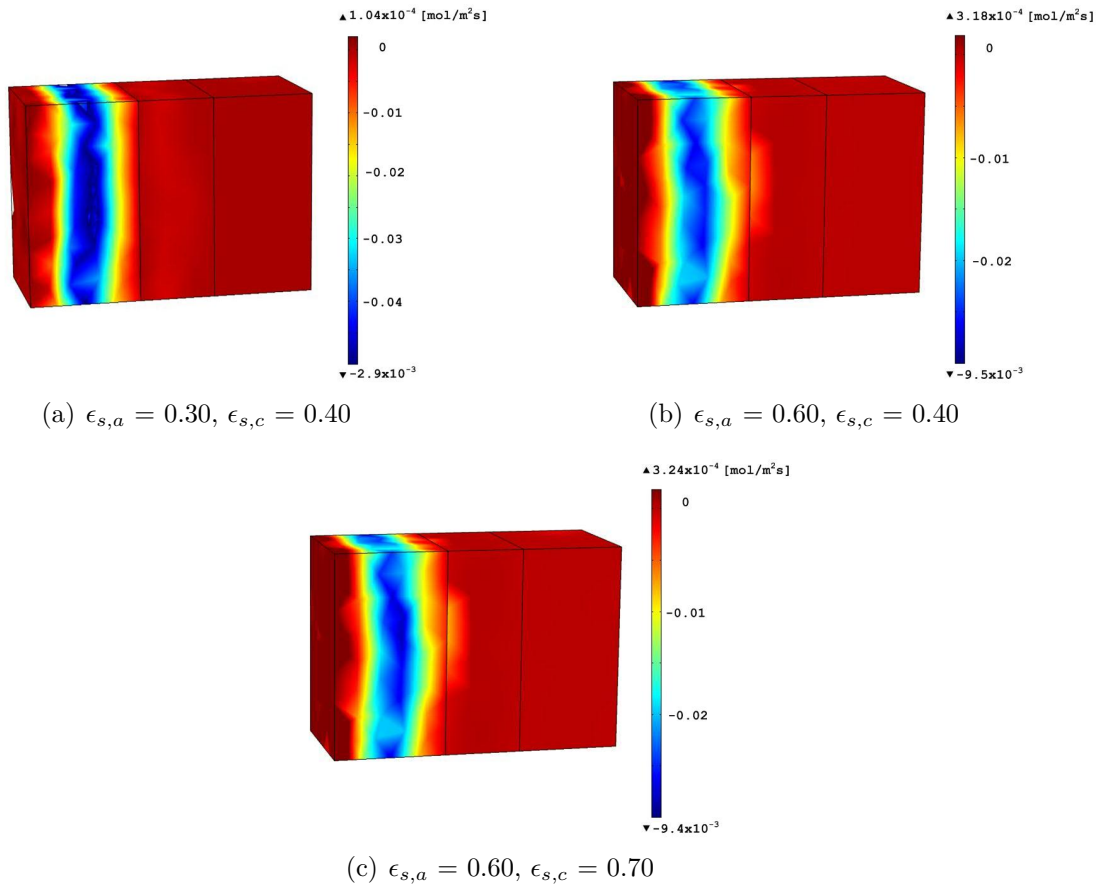


**Figure 6.14: Lithium ion concentration in the electrolyte for different volume fractions**

The flux of lithium ions, for all volume fraction values, was surprisingly low in the anode region compared to the other domains (see figure 6.14). The higher the volume fractions of the solid phases was, the lower was the lithium ion flux in the anode. This was caused by the lower diffusion coefficient of the solid phase, which led to less lithium atoms diffusing to the electrode/electrolyte interface and reacting to lithium ions.

## 6.4 Length variation

The length of the separator was varied between  $4 \cdot 10^{-5}$  and  $9 \cdot 10^{-5}$  m, to evaluate the impacts on the lithium ion cell model.

It was expected that if the separator region was smaller, the border of intercalation/de-intercalation was displaced more into the inner direction of the electrodes.

### 6.4.1 Lithium concentration in the solid phase

In this approach, the variation of the separator length had the greatest effect on the electrochemical model.

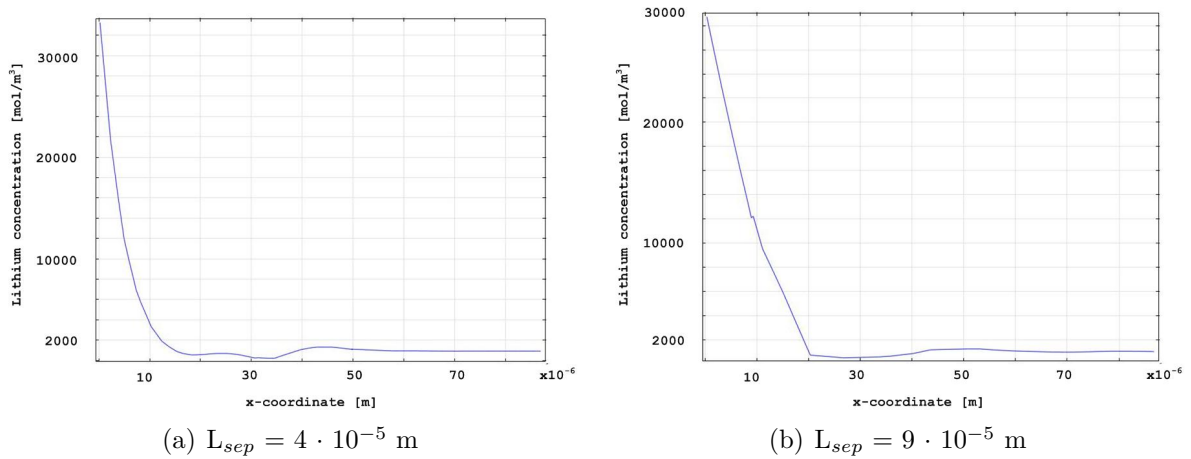


**Figure 6.15: Lithium concentration in the solid phase of the anode for different separator lengths**

The intercalation of lithium into the solid phase of the anode took place at round  $40 \cdot 10^{-6}$  m when the separator was smaller, and at round  $43 \cdot 10^{-6}$  m when the separator was larger (see figure 6.15). Generally, the lithium concentration in the anode was lower for the larger separator region.

The lithium concentration in the solid phase of the cathode didn't vary for different separator lengths. The slight discrepancies of the values were natural oscillations and not classifiable as significant changes.

### 6.4.2 Lithium concentration in the liquid phase

The lithium ion concentration in the electrolyte varied strongly for the different separator lengths (see figure 6.16).

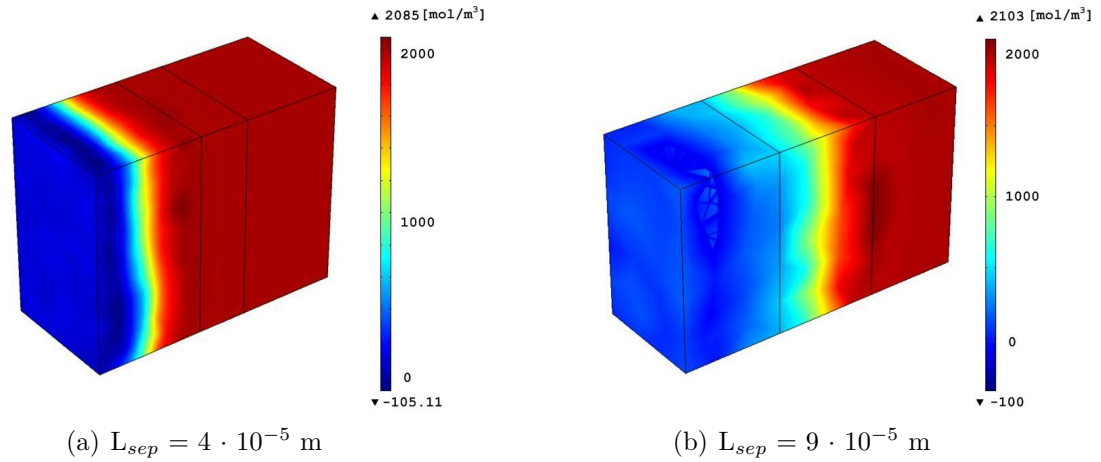


**Figure 6.16:** Lithium ion concentration in the electrolyte for different separator lengths

When the separator region was small, the lithium ions could easier diffuse and migrate from the positive to the negative electrode. Therefore, the border between higher and lower concentration in the electrolyte was in the inner side of the anode.

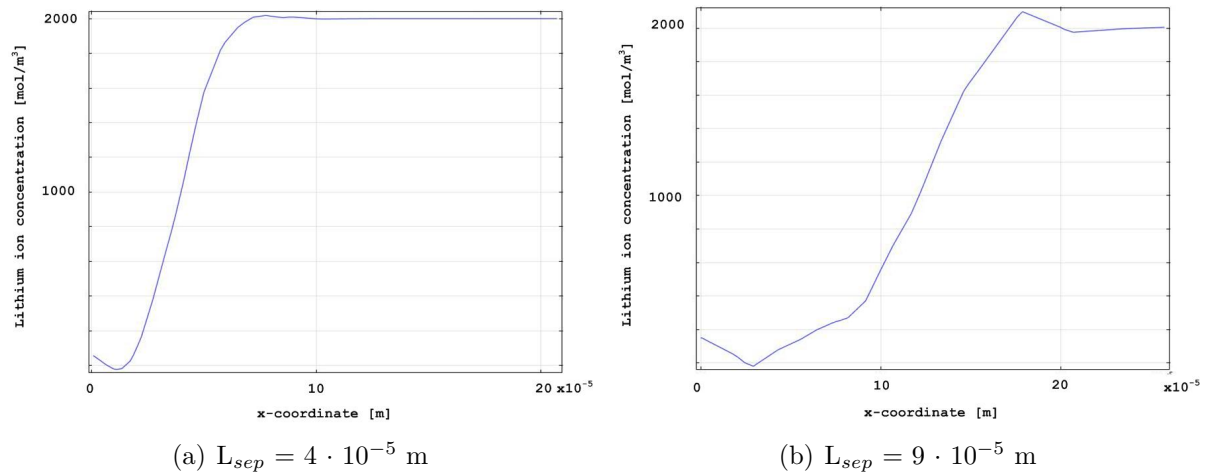


**Figure 6.17:** Lithium ion concentration in the electrolyte for different separator lengths, x-axis

If the separator region was large, the route of lithium transport was larger as well and within the first 10 s of charging, the border between high and low concentration regions only reached the middle of the separator (see figure 6.17).

### 6.4.3 Lithium ion flux

The lithium ion flux also varied significantly for different separator length scales (see figure 6.18).

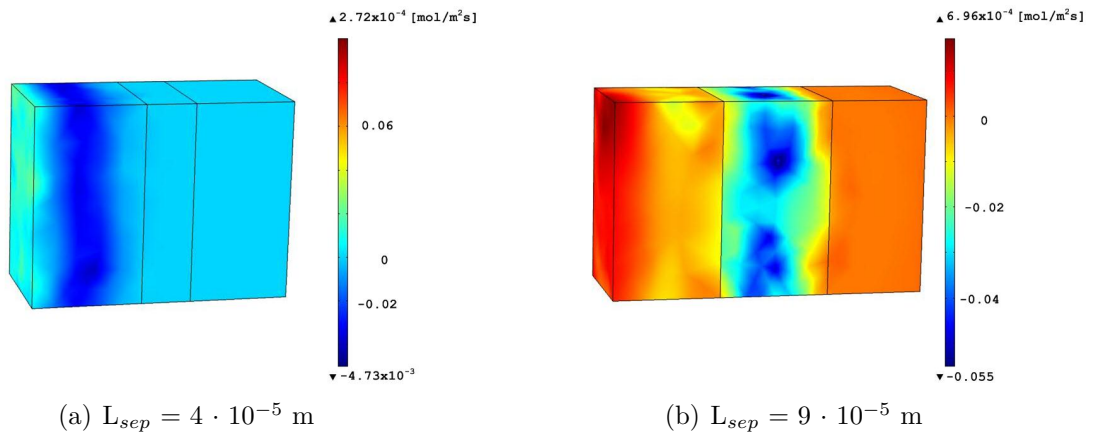
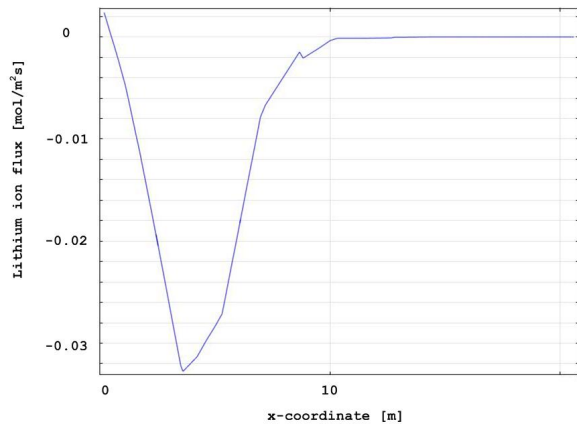


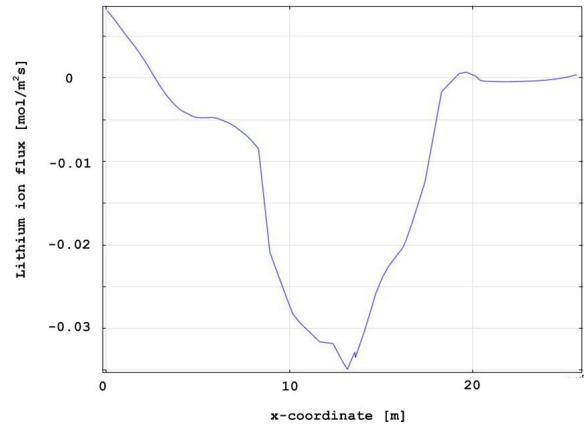
**Figure 6.18: Lithium ion concentration in the electrolyte for different separator lengths, x-coordinate**

When the separator region was small, the flux was quite uniform over the cell. The only difference was the domain of the anode, in which center the flux reached a minimum. This pictured that the lithium ions, which diffused and migrated to the negative electrode, reacted at the surfaces of the particles and were intercalated into the graphite material.

The results for the larger separator showed a flux minimum in the middle of the cell. This seemed strange but was caused by the slowed flux due to large transport routes (see figure 6.19).



(a)  $L_{sep} = 4 \cdot 10^{-5} \text{ m}$



(b)  $L_{sep} = 9 \cdot 10^{-5} \text{ m}$

**Figure 6.19: Lithium ion concentration in the electrolyte for different separator lengths, x-axis**

# 7 Conclusions and further perspective

## 7.1 Conclusions

In this master thesis was shown how to create an electrochemical three-dimensional battery cell model using a conventional simulation software. COMSOL Multiphysics solves models using the so-called finite element analysis, which is a quite popular method of discretization. The model geometry was a rectangular detail of a conventionally lithium ion battery. It was shown how to create and compute a model with different cell parameters.

The finite element method is an important tool nowadays. However, its application in a commercial software is a delicate issue. A fundamental understanding of the analysis and method of discretization is important to derive meaningful results and reliable data.

The parameter variation determined the effect of some parameters on the electrochemical cell. The presented results showed that the influence of the particle size in a monodisperse matrix has less influence than the porosity of the electrodes. Within the first 10 s of charging, the length of the separator had the highest impact into the lithium ion battery model.

The results are in a good agreement with state-of-the-art battery models. The one-dimensional model showed how the concentration of lithium ions in the electrolyte rises at the electrode, where lithium is de-intercalated, and drops at the electrode where lithium is intercalated. This effect is also visible in the presented three-dimensional electrochemical model. *Q.-f. Liu et al.* showed that the variation of the ionic concentration over the y-axis is not significant, which is also demonstrated in this thesis.

*In situ* measurements by *S. J. Harris et al.* demonstrated that the intercalation process first takes place at this side of the electrode, which is exposed to the separator and closer to the counter electrode. The longer the charging/discharging process takes, the more the border of intercalation is moving into the inner side of the electrode. This situation is also displayed in the results of the three-dimensional simulation and the border of intercalation is visible in the data

The simulation of 3D-microbatteries by *V. Zadin* and *D. Brandell* have shown how the variation of the distance between the electrodes impacts the concentration profiles in the electrolyte. Because zero separator resistance is assumed in the model in this thesis, the results are comparable. The concentration differs more for the shorter distance, which is the same result as in this electrochemical model. For the polymer electrolyte, this effect is even stronger due to worse transport properties of the ions.

Because of the good conformance between the three-dimensional electrochemical model of the lithium ion cell and the state-of-the-art battery models, the model is feasible and the data is assumed to be reliable.

## **7.2 Further perspective**

As mentioned before, the validation of a model is one of the most important things. Even if some values are difficult to derive, it is necessary to validate the simulation. Therefore, the measuring of the derived results via different tools, has to be done. To perform this, the electrochemical model should be transferred to a conventional lithium ion battery and the data of the measurements should be compared with the model outputs.

Additionally, other processes or side reactions inside the cell, which have been neglected, can be added. The results could be compared with those from the simple model and the effect of the process on the model can be evaluated.

In this thesis, only parameters have been varied which don't (or little) affect other cell properties (for example, temperature variation would influence also the cell reaction rate). But different cell materials and their parameters could also be inserted into the model to derive their effect on the performance of the cell.

# Bibliography

- [1] J. Garche, editor. *Encyclopedia of electrochemical power sources*, volume 5. Elsevier B.V., 2009.
- [2] M. K. Hughes R. S. Bradley S. K. Miller S. Rutherford M. E. Mann, Z. Zhang and F. Ni. Proxy-based reconstructions of hemispheric and global surface temperature variations over the past two millennia. *PNAS*, 105:13252–13257, 2008.
- [3] J. Weber. *Automotive development processes*. Springer-Verlag Berlin Heidelberg, 2009.
- [4] S. De S. Santhanagopalan R. D. Braatz V. R. Subramanian V. Ramadesigan, P. W. C. Northrop. Modeling and simulation of lithium-ion batteries from a systems engineering perspective. *Journal of the Electrochemical Society*, 159 (3):R31–R45, 2012.
- [5] K. E. Thomas-Alyea J. Newman. *Electrochemical systems*. John Wiley & Sons, 3rd edition, 2004.
- [6] K. A. Smith. *Electrochemical modeling, estimation and control of lithium ion batteries*. PhD thesis, The Pennsylvania State University, The Graduate School, Department of Mechanical and Nuclear Engineering, 2006.
- [7] R. E. White G. G. Botte, V. R. Subramanian. Mathematical modeling of secondary lithium batteries. *Electrochimica Acta*, 45:2595–2609, 2000.
- [8] J. O. Besenhard, editor. *Handbook of battery materials*. John Wiley & Sons, 1999.
- [9] R. E. White S. K. Rahimian, S. Rayman. Comparison of single particle and equivalent circuit analog models for a lithium-ion cell. *Journal of Power Sources*, 196:8450–8462, 2011.
- [10] P. H. L. Notten H. J. Bergveld, W. S. Kruijt. *Battery Management Systems - design by modelling*. Kluwer Academic Publishers, 2002.
- [11] J. Vogel S. Käbitz F. Hust P. Dechent D. U. Sauer M. Ecker, J. B. Gerschler. Development of a lifetime prediction model for lithium-ion batteries based on extended accelerated aging test data. *Journal of Power Sources*, 215:248–257, 2012.
- [12] P. Ramadass R. E. White S. Santhanagopalan, Q. Guo. Review of models for predicting the cycling performance of lithium ion batteries. *Journal of Power Sources*, 156:620–628, 2006.

- [13] B. Schweighofer M. Cifrain M. S. Sommer, D. Hrach. Fast algorithm for calculating the surface concentration of spherical particles for lithium-ion battery simulations. *Procedia Engineering*, 5:389–392, 2010.
- [14] A. W. Imre L. Guzzella A. P. Schmidt, M. Bitzer. Experiment-driven electrochemical modeling and systematic parameterization for a lithium-ion battery cell. *Journal of Power Sources*, 195:5071–5080, 2010.
- [15] R. E. White M. Guo, G. Sikha. Single-particle model for a lithium-ion cell: thermal behavior. *Journal of the Electrochemical Society*, 158 (2):A122–A132, 2011.
- [16] R. E. White S. K. Rahimian, S. Rayman. Comparison of single particle and equivalent circuit analog models for a lithium-ion cell. *Journal of Power Sources*, 196:8450–8462, 2011.
- [17] L. Alvarez-Icaza A. Romero-Becerril. Comparison of discretization methods applied to the single-particle model of lithium-ion batteries. *Journal of Power Sources*, 196:10267–10279, 2011.
- [18] H. Hafezi D. R. Wheeler J. Newman, K. E. Thomas. Modeling of lithium-ion batteries. *Journal of Power Sources*, 119-121:838–843, 2003.
- [19] J. Newman M. Doyle, T. F. Fuller. Modeling of galvanostatic charge and discharge of the lithium/polymer/insertion cell. *Journal of the Electrochemical Society*, 140 (6):1526–1533, 1993.
- [20] F. Ciucci W. Lai. Mathematical modeling of porous battery electrodes - revisit of newman’s model. *Electrochimica Acta*, 56:4369–4377, 2011.
- [21] R. Purkayastha R. M. McMeeking. Models for li-ion battery performance and damage. In *8th European Solid Mechanics Conference, Graz*, 9th July 2012.
- [22] Y. Cui E. Wang W. Wan, Q. Zhang. First principles study of lithium insertion in bulk silicon. *Journal of Physics: Condensed Matter*, 22:415501–415510, 2010.
- [23] V. B. Shenoy S.-P. Kim, A. C. T. Duin. Effect of electrolytes on the structure and evolution of the solid electrolyte interphase (sei) in li-ion batteries: A molecular dynamics study. *Journal of Power Sources*, 196:8590–8597, 2011.
- [24] J. McPhee T.-S. Dao, C. P. Vyasarayani. Simplification and order reduction of lithium-ion battery model based on porous-electrode theory. *Journal of Power Sources*, 198:329–337, 2012.
- [25] D. R. Baker C. Monroe S. J. Harris, A. Timmons. Direct in situ measurements of lithium transport in li-ion battery negative electrodes. *Chemical Physics Letters*, 485:265–274, 2010.
- [26] D. Brandell P. H.L. Notten A. Aabloo V. Zadin, D. Danilov. Finite element simulations of 3d ionic transportation properties in li-ion electrolytes. *Electrochimica Acta*, 65:165–173, 2012.

- [27] D. Brandell V. Zadin. Modeling polymer electrolytes for 3d-microbatteries using finite element analysis. *Electrochimica Acta*, 57:237–243, 2011.
- [28] X. Zhang A.M. Sastry Y-H. Chen, C.-W. Wang. Porous cathode optimization for lithium cells: Ionic and electronic conductivity, capacity, and selection of materials. *Journal of Power Sources*, 195:2851–2862, 2010.
- [29] P. Fröhlich. *FEM-Leitfaden*. Springer-Verlag Berlin Heidelberg, 1995.
- [30] D. Suess. Finite elemente methode. Lecture Notes Computational Physics, June 2003. Technical University of Vienna.
- [31] COMSOL Multiphysics. *Reference guide*, 4.3 edition, 2012.
- [32] P. Boeraeve. Introduction to the finite element method (fem). Lecture Notes Haute Ecole Libre Mosane, Jan. 2010.
- [33] K.-J. Bathe. *Finite-Elemente-Methoden*. Springer-Verlag Berlin Heidelberg, 2 edition, 2002.
- [34] COMSOL Multiphysics. *Edge effects in a spirally wound li-ion battery*, 4.3 edition, 2012.
- [35] S.-Y. Choe M. Xiao. Dynamic modeling and analysis of a pouch type  $\text{limn}_2\text{o}_4$ /carbon high power li-polymer battery based on electrochemical-thermal principles. *Journal of Power Sources*, 218:357–367, 2012.
- [36] U. Shumlak W. Lowrie, V. S. Lukin. A priori mesh quality metric error analysis applied to a high-order finite element method. *Journal of Computational Physics*, 230:5564–5586, 2011.
- [37] L. R. Faulkner A. J. Bard. *Electrochemical methods - fundamentals and applications*. John Wiley & Sons, 2nd edition, 2001.
- [38] P. Novák O. Haas E. Deiss, D. Häring. Modeling of the charge-discharge dynamics of lithium manganese oxide electrodes for lithium-ion batteries. *Electrochimica Acta*, 46:4185–4196, 2001.
- [39] R. E. White L. Cai. Mathematical modeling of a lithium ion battery with thermal effects in comsol inc. multiphysics (mp) software. *Journal of Power Sources*, 196:5985–5989, 2011.
- [40] COMSOL Multiphysics. *1D Isothermal lithium-ion battery*, 4.3 edition.
- [41] A. H. Wiedemann R. J. Kee G. M. Goldin, A. M. Colclasure. Three-dimensional particle-resolved models of li-ion batteries to assist the evaluation of empirical parameters in one-dimensional models. *Electrochimica Acta*, 64:118–129, 2012.
- [42] COMSOL Multiphysics. *User’s guide*, 4.3 edition, 2012.

- [43] P. M. Gomadam R. White B. N. Popov P. Ramadass, B. Haran. Development of first principles capacity fade model for li-ion cells. *Journal of the Electrochemical Society*, 151 (2):A196–A203, 2004.

# List of Figures

2.1	Scheme of a conventional lithium ion battery . . . . .	4
2.2	Discharge process of a lithium ion cell . . . . .	5
2.3	Electronic network for a lithium ion cell . . . . .	6
2.4	Schematic view of the three different models . . . . .	8
2.5	State of lithium intercalation . . . . .	11
2.6	Lithium ion concentration in the electrolyte . . . . .	12
2.7	Concentration gradient in the electrolyte for different electrode distances	13
2.8	Influence of the porosity on the ionic and electronic conductivity . . . . .	14
2.9	Linear basis function set . . . . .	16
2.10	Connection between local and global coordinates . . . . .	17
2.11	Lagrange element - Quadratic tetrahedron . . . . .	17
3.1	Spirally wound battery . . . . .	20
3.2	Pouch cell geometry . . . . .	21
3.3	Different meshes of the simulated model . . . . .	21
3.4	Statistics of the coarse mesh element quality . . . . .	22
3.5	Statistics of the normal mesh element quality . . . . .	24
4.1	Equilibrium potential of the anode . . . . .	29
4.2	Equilibrium potential of the cathode . . . . .	29
5.1	COMSOL desktop of the electrochemical model . . . . .	31
5.2	Feature nodes of the <i>Convection-Diffusion Equation</i> interface . . . . .	33
5.3	Example for a feature node, its settings and boundary selection . . . . .	34
5.4	Default view of the model builder window . . . . .	36
5.5	Geometry settings window . . . . .	36
5.6	Interpolation of the data to define the anode potential function . . . . .	37
5.7	Settings of the <i>Convection-Diffusion Equation</i> feature node . . . . .	38
5.8	Settings of the <i>Parametric Sweep</i> node . . . . .	40
6.1	Lithium concentration in the solid phase of the electrodes . . . . .	41
6.2	Lithium concentration in the solid phase of the anode . . . . .	42
6.3	Lithium concentration in the solid phase of the cathode . . . . .	42
6.4	Lithium ion concentration in the electrolyte . . . . .	43
6.5	Lithium ion concentration in the electrolyte, x-axis . . . . .	43
6.6	Lithium ion flux, x-coordinate . . . . .	44
6.7	Lithium ion flux, x-axis . . . . .	44
6.8	Lithium concentration in the solid phase of the electrodes for different particle sizes . . . . .	45
6.9	Lithium concentration in the solid phase for different particle sizes, x-axis	46

6.10	Lithium ion flux, x-axis . . . . .	47
6.11	Lithium concentration in the solid phase of the anode for different volume fractions, x-axis . . . . .	49
6.12	Lithium concentration in the solid phase of the cathode for different volume fractions, x-axis . . . . .	50
6.13	Lithium ion concentration in the electrolyte for different volume fractions	51
6.14	Lithium ion concentration in the electrolyte for different volume fractions	52
6.15	Lithium concentration in the solid phase of the anode for different separator lengths . . . . .	53
6.16	Lithium ion concentration in the electrolyte for different separator lengths	54
6.17	Lithium ion concentration in the electrolyte for different separator lengths, x-axis . . . . .	54
6.18	Lithium ion concentration in the electrolyte for different separator lengths, x-coordinate . . . . .	55
6.19	Lithium ion concentration in the electrolyte for different separator lengths, x-axis . . . . .	56

# A Appendix

## A.1 Parameter setup

Parameter	Value
$L_a$ [m] <sup>b</sup>	$88 \cdot 10^{-6}$
$L_{sep}$ [m] <sup>a</sup>	$60 \cdot 10^{-6}$
$L_c$ [m] <sup>b</sup>	$80 \cdot 10^{-6}$
$D_{cell}$ [m] <sup>a</sup>	$100 \cdot 10^{-6}$
$H_{cell}$ [m] <sup>a</sup>	$160 \cdot 10^{-6}$
$T$ [K] <sup>a</sup>	298
$I_{app}$ [A] <sup>a</sup>	$1.6 \cdot 10^{-7}$
$R_a$ [m] <sup>b</sup>	$2 \cdot 10^{-6}$
$R_c$ [m] <sup>b</sup>	$2 \cdot 10^{-6}$
$\epsilon_{s,a}$ [none] <sup>b</sup>	0.49
$\epsilon_{s,c}$ [none] <sup>b</sup>	0.59
$\epsilon_{l,a}$ [none] <sup>b</sup>	0.485
$\epsilon_{l,c}$ [none] <sup>b</sup>	0.365
$c_{s,a_{max}}$ [molm <sup>-3</sup> ] <sup>b</sup>	30555
$c_{s,a_0}$ [molm <sup>-3</sup> ] <sup>b</sup>	$0.03 \cdot c_{s,a_{max}}$
$c_{s,c_{max}}$ [molm <sup>-3</sup> ] <sup>b</sup>	51555
$c_{s,c_0}$ [molm <sup>-3</sup> ] <sup>b</sup>	$0.95 \cdot c_{s,c_{max}}$
$c_{l,0}$ [molm <sup>-3</sup> ] <sup>a</sup>	2000
$D_{s,a}$ [m <sup>2</sup> s <sup>-1</sup> ] <sup>b</sup>	$3.9 \cdot 10^{-14}$
$D_{s,c}$ [m <sup>2</sup> s <sup>-1</sup> ] <sup>b</sup>	$1 \cdot 10^{-14}$
$D_{l,Li^+}$ [m <sup>2</sup> s <sup>-1</sup> ] <sup>b</sup>	$7.5 \cdot 10^{-10}$
$D_{l,PF_6^-}$ [m <sup>2</sup> s <sup>-1</sup> ] <sup>a</sup>	$8 \cdot 10^{-10}$
$\sigma_{s,a}$ [Sm <sup>-1</sup> ] <sup>b</sup>	100
$\sigma_{s,c}$ [Sm <sup>-1</sup> ] <sup>b</sup>	100
$brugg_a$ [none] <sup>b</sup>	4
$brugg_c$ [none] <sup>b</sup>	4
$\alpha_a$ [none] <sup>b</sup>	0.5
$\alpha_c$ [none] <sup>b</sup>	0.5
$k_{a_0}$ [s <sup>-1</sup> ] <sup>c</sup>	$4.854 \cdot 10^{-6}$
$k_{c_0}$ [s <sup>-1</sup> ] <sup>c</sup>	$2.252 \cdot 10^{-6}$

<sup>a</sup> Assumed

<sup>b</sup> From literature [12]

<sup>c</sup> From literature [43]

## A.2 Feature nodes

### A.2.1 Convection-Diffusion Equation

(twice - anode/cathode)

- *Convection-Diffusion Equation* (Domain)
- *Zero Flux* (Exterior boundaries)
- *Initial Values* (Domain)
- *Lithium flux* (Interior boundary)
- *Concentration derivate* (Boundary - current collector)
- *Electric ground* (Boundary - current collector)
- *Potential derivate* (Interior boundary)
- *Current density* (Boundary - current collector)

### A.2.2 Transport of Diluted Species

- *Diffusion separator* (Domain)
- *Initial values* (Domain)
- *No PF6 flux separator* (Exterior boundaries)
- *No Li flux separator* (Exterior boundaries)
- *No reaction separator* (Domain)
- *Charge balance separator* (Domain)
- *Diffusion anode* (Domain)
- *Diffusion cathode* (Domain)
- *No PF6 flux anode* (Exterior boundaries)
- *No Li flux anode* (Exterior boundaries)
- *No PF6 flux cathode* (Exterior boundaries)
- *No Li flux cathode* (Exterior boundaries)
- *Concentration derivate* (Boundary - current collector)
- *Potential derivate anode* (Boundary - current collector)
- *Potential derivate cathode* (Boundary - current collector)

- *Charge balance anode* (Domain)
- *Charge balance cathode* (Domain)
- *Lithium flux anode* (Interior boundary)
- *Lithium flux cathode* (Interior boundary)
- *Reaction anode* (Domain)
- *Reaction cathode* (Domain)
- *Liquid flux similarity anode x* (Interior boundary)
- *Liquid flux similarity anode y* (Interior boundary)
- *Liquid flux similarity anode z* (Interior boundary)
- *Liquid flux similarity cathode x* (Interior boundary)
- *Liquid flux similarity cathode y* (Interior boundary)
- *Liquid flux similarity cathode z* (Interior boundary)
- *Liquid current density similarity anode x* (Interior boundary)
- *Liquid current density similarity anode y* (Interior boundary)
- *Liquid current density similarity anode z* (Interior boundary)
- *Liquid current density similarity cathode x* (Interior boundary)
- *Liquid current density similarity cathode y* (Interior boundary)
- *Liquid current density similarity cathode z* (Interior boundary)
- *Current density* (Boundary - current collector)